New Journal of Physics
The open-access journal for physics

Study of photo-proton reactions driven by bremsstrahlung radiation of high-intensity laser generated electrons

K M Spohr[1,5], M Shaw[1], W Galster[2], K W D Ledingham[2,3,4], L Robson[2,3], J M Yang[2,6], P McKenna[2], T McCanny[2], J J Melone[1], K-U Amthor[4], F Ewald[4,7], B Liesfeld[4], H Schwoerer[4,8] and R Sauerbrey[4,9]

[1] SUPA, School of Engineering and Science, University of the West of Scotland, High Street 1, Paisley PA1 2BE, UK
[2] SUPA, Department of Physics, University of Strathclyde, Rottenrow, Glasgow G4 0NG, UK
[3] AWE plc, Aldermaston, Reading RG7 4PR, UK
[4] Institut für Optik und Quantenelektronik, Friedrich-Schiller-Universität Jena, Max-Wien-Platz 1, 07743 Jena, Germany
E-mail: klaus.spohr@uws.ac.uk

New Journal of Physics **10** (2008) 043037 (25pp)
Received 13 December 2008
Published 22 April 2008
Online at http://www.njp.org/
doi:10.1088/1367-2630/10/4/043037

Abstract. Photo-nuclear reactions were investigated using a high power table-top laser. The laser system at the University of Jena ($I \sim 3$–$5 \times 10^{19}\,\mathrm{W\,cm^{-2}}$) produced hard bremsstrahlung photons ($kT \sim 2.9\,\mathrm{MeV}$) via a laser–gas interaction which served to induce (γ, p) and (γ, n) reactions in Mg, Ti, Zn and Mo isotopes. Several (γ, p) decay channels were identified using nuclear activation analysis to determine their integral reaction yields.

[5] Author to whom any correspondence should be addressed.
[6] Present address: Research Center of Laser Fusion, China Academy of Engineering Physics, PO Box 919-986, 621900 Miangyang, People's Republic of China.
[7] Present address: Laboratoire d'Optique Appliquée, École Polytechnique, ENSTA, CNRS, UMR 7639, 91761 Palaiseau, France.
[8] Present address: Laser Research Institute, University of Stellenbosch, Private Bag X1, 7602 Matieland, South Africa.
[9] Present address: Forschungszentrum Rossendorf e.V., PO Box 510119, Bautzner Landstr. 128, 01328 Dresden, Germany.

As the laser-generated bremsstrahlung spectra stretches over the energy regime dominated by the giant dipole resonance (GDR), these yield measurements were used in conjunction with theoretical estimates of the resonance energies E_{res} and their widths Γ_{res} to derive the integral reaction cross-section $\sigma^{\mathrm{int}}(\gamma, \mathrm{p})$ for ^{25}Mn, ^{48,49}Ti, ^{68}Zn and ^{97,98}Mo isotopes for the first time. This study enabled the determination of the previously unknown $\frac{\sigma^{\mathrm{int}}(\gamma,\mathrm{n})}{\sigma^{\mathrm{int}}(\gamma,\mathrm{p})}$ cross-section ratios for these isotopes. The experiments were supported by extensive model calculations (EMPIRE) and the results were compared to the Thomas–Reiche–Kuhn (TRK) dipole sum rule as well as to the experimental data in neighboring isotopes and good agreement was observed. The Coulomb barrier and the neutron excess strongly influence the $\frac{\sigma^{\mathrm{int}}(\gamma,\mathrm{n})}{\sigma^{\mathrm{int}}(\gamma,\mathrm{p})}$ ratios for increasing target proton and neutron numbers.

Contents

1. Introduction

In this decade, the development of new laser systems capable of producing ultra-high intensities in the region of $10^{19-21}\,\mathrm{W\,cm^{-2}}$ has created a new field of research at the interface of laser–plasma and nuclear physics. As a result of a series of technological breakthroughs, nuclear research facilitating high powered laser systems has established itself as a successful complementary route to traditional accelerator-based nuclear physics. A series of experiments have been performed that exploit the unique features of laser-generated ultra-short high brightness pulses of MeV particles and radiation. Currently high-intensity laser systems are capable of accelerating protons up to $\sim$60 MeV [1]–[4] and heavy ions into the regime of several megaelectronvolts (MeV) per nucleon [5] and these energies are sufficient to induce nuclear reactions in secondary targets [6]–[8]. Recently, further progress with respect to the laser-induced acceleration of electrons has been reported by several groups [9, 10] and as of early 2008 scientists are able to create bursts of highly energetic electrons with energies of up to 1 GeV by wakefield acceleration in gas targets [11]. The use of a secondary high-Z converter target permits the conversion of these relativistic electrons into high-energy bremsstrahlung photons with energies in the MeV range [12]. This radiation can be employed to induce photo-nuclear reactions such as (γ, n), (γ, p) or (γ, f) on selected targets. Inspired by the theoretical work of Boyer *et al* [13] the photo-induced fission of heavy elements was first demonstrated

on a natural uranium target in 2000 by a single $10^{20}\,\mathrm{W\,cm^{-2}}$ laser pulse from the VULCAN facility at the Rutherford Appleton Laboratory [14] and by a similar experiment at the Lawrence Livermore National Laboratory [15]. Soon after these developments, the Jena table-top high repetition rate laser was used to successfully show the induced fission of actinides by integrating over several hundred $10^{19}\,\mathrm{W\,cm^{-2}}$ laser pulses [16]. In addition, bremsstrahlung radiation of laser-accelerated electrons has been used to induce $(\gamma, x\mathrm{n})$ reactions to be facilitated as a diagnostic tool. This technique allows e.g. to determine the temperature of the laser-accelerated electron-induced photon spectra, where conventional methods such as dose measurements and thermoluminescence are not applicable [17, 18]. Furthermore, in 2002 an important application for lasers was reported in inaugural studies of transmutation reactions relevant for nuclear waste management [19, 20]. In these studies, the transmutation of the β^--decaying waste product ^{129}I ($t_{1/2} \sim 15.7 \times 10^6$ years) was successfully demonstrated by inducing the photo-nuclear reaction $^{129}\mathrm{I}(\gamma, \mathrm{n})^{128}\mathrm{I}$. The final product of the reaction ^{128}I decays with $t_{1/2} \sim 25.0$ min, which is 3.3×10^{11} times shorter than the half-life of its mother nuclei. Importantly, these studies also provided the first experimental measurement of the integrated photo-neutron cross-section $\sigma^{\mathrm{int}}(\gamma, \mathrm{n})$ for ^{129}I. In this paper, a detailed investigation of the photon-induced reactions with a high-intensity ($I \sim 10^{19}\,\mathrm{W\,cm^{-2}}$), multi-terawatt laser is reported. The reaction yields of photo-nuclear activation of a range of nuclei were extracted and integral (γ, n) and (γ, p) cross-sections were derived. Although there has been a number of (γ, n) measurements using bremsstrahlung radiation of laser-accelerated electrons, much less work on (γ, p) reactions has been carried out with this method. Stoyer *et al* [21] have predicted that once laser performance is more reproducible, better estimates of (γ, p) cross-sections may be possible. The present paper was written to substantiate this suggestion over a range of isotopes in certain elements, namely magnesium, titanium, zinc and molybdenum, thereby demonstrating that university-scale laser systems are well suited for the experimental study of important photo-nuclear reactions.

2. Photo-nuclear reactions and new possibilities for high-intensity laser research

Photo-nuclear data are of great importance for a variety of current and emerging applications, such as radiation shielding design, radiation transport analysis, radiotherapy, fission and fusion reactor development and, as depicted above, nuclear transmutation. New data on photo-nuclear reactions are furthermore helping the nuclear astrophysics community in their ongoing quest to better understand the details of nucleo-synthesis, one of the most prominent questions in modern physics research [22]. For applied and fundamental research the giant dipole resonance (GDR) region, extending up to $\sim$40 MeV, is of greatest importance. Despite a series of international projects targeting the systematic study of photon-induced nuclear reactions in the GDR regime, there is still a significant lack of suitable photo-nuclear data. This problem has been highlighted by the International Atomic Energy Agency (IAEA) which points out that the shortfall in current knowledge hinders any progress in the development of transport simulation codes [23] and dose calculations for photon therapy [24]. The latest IAEA report [25] lists around 40 materials for which photo-nuclear data are urgently needed. Emphasis is given to elements that are used as bremsstrahlung converters and in structural shielding: Ti, Fe, Cu, Zn and Mo, as well as biological and fissionable materials (C, N, O; Th, U, Pu,...). In the same report, an evaluated photo-nuclear cross-section library is presented, which combines extensive research activities of a series of institutions worldwide such as MSU Moscow, LANL Los Alamos, CEN Saclay and the LNL Livermore [26]. The evaluated cross-section data for around 170 isotopes presented

in this publication are included in the EXFOR database of the National Nuclear Data Center (NNDC) [27]. The IAEA report highlights especially the deficiency of data for charged particle emission channels and all prominent databases together hold information for only $\sim$260(γ, p) experiments at present. The majority of these measurements concentrate on very light systems such as ^{3,4}He or ^{7}Li and only a little more than 40 different isotopes have been catalogued with regard to photo-induced proton emission. As bremsstrahlung photons generated by table-top multi-terawatt lasers extend over several tens of MeV, such high-intensity laser systems are suited to comprehensive experimental programs focusing on (γ, n) and (γ, p) reaction cross-sections for a wide range of stable nuclei. The present study demonstrates the use of high power lasers in this regard and contributes substantial new information on photo-nuclear physics research.

Over the last four decades, great efforts have been undertaken in order to simulate photo-nuclear reactions with the aim of predicting the magnitude and energy dependence of the cross-section $\sigma(E)$ by achieving a best fit to experimental data. The codes EMPIRE [28] and GNASH [29] have become a standard tool for such investigations. The underlying models have to account for the different reaction mechanisms involved in the photo-nuclear excitation process and in the subsequent decay of the excited nucleus by particle and γ-ray emission. At low energies ($E < 40$ MeV) the GDR is by far the dominant photon absorption mechanism and the total photo-reaction cross-section $\sigma(\gamma, \mathrm{tot})$ is similar to σ_{GDR}. The GDR is seen to be a collective bulk oscillation of neutrons against protons resulting in the emission of light particles and high-energy γ-rays. The energy dependence of the GDR component $\sigma_{\mathrm{GDR}}(E)$ is in good approximation described by the superposition of Lorentzians with energy-dependent widths $\Gamma_{\mathrm{res}(i)}$:

$$\sigma_{\mathrm{GDR}}(E) = \sum_i \sigma_{\mathrm{res}(i)} \frac{(E\Gamma_{\mathrm{res}(i)})^2}{(E^2 - E_{\mathrm{res}(i)}^2)^2 + (E\Gamma_{\mathrm{res}(i)})^2}, \tag{1}$$

where $\sigma_{\mathrm{res}(i)}$ and $E_{\mathrm{res}(i)}$ are the GDR resonance cross-sections and energies, respectively. For spherical and near-spherical nuclei one resonance is dominating and $i = 1$, whereas deformed nuclei exhibit two distinct resonances. The threshold energy E_{th} is given by the reaction Q-value. EMPIRE uses fits to experimental data to derive these parameters for a specific isotope based on the Dietrich–Berman evaluations [30] or from systematical trends seen in neighboring nuclei. In order to retrieve an experimental value for the integrated cross-section $\sigma^{\mathrm{int}} \sim \int_{E_{\mathrm{th}}}^{\sim 40\,\mathrm{MeV}} \sigma(E)\,\mathrm{d}E$ from activation measurements, a knowledge of these parameters is crucial. It should be pointed out that EMPIRE includes the presence of lower-lying small-scale resonances if such data exist for an isotope. Furthermore, pre-equilibrium particle emission is accounted for as well.

From an experimental point of view, one of the main reasons for the shortfall in the knowledge of photo-proton reactions lies in the fact that direct studies of reactions involving charged particles require in general a greater experimental effort than investigations on neutron emission. A charged particle detection system has to be placed inside the vacuum in proximity to the interaction region, while neutron detectors can be placed outside in air. As an alternative to the direct detection of the emitted particles, activity measurements on radioactive residual nuclei produced by γ-induced reactions can be employed for examining (γ, p) reactions in many isotopes. By using high-purity intrinsic germanium (Ge-)detectors the characteristic energy and decay-time pattern of nuclear transitions are measured with high precision, allowing a determination of reaction yields and hence the cross-sections for the initiating photon processes.

Limitations of this procedure are the restricted number of stable isotopes that transmute into detectable radioactive species and the possible onset of multiparticle emission in heavier target isotopes which may lead to the same radioactive end product.

Previous investigations have shown the feasibility of using photons emerging from a relativistic laser-produced plasma to investigate photo-nuclear reactions in combination with the activation method [31]. Because of the short duration and the small size of the very strong accelerating fields ($|\vec{E}| \sim 10^{11}$ V cm^{-1}, $|\vec{B}| \sim 10^{9}$ G) the particle source is of extreme brilliance in spatial and temporal terms. The activation method is a suitable detection technique for the off-line examination of (γ, p) reactions. In 2001, Stoyer *et al* [21] have successfully used this method for the measurement of the integral $\frac{\sigma^{\mathrm{int}}(\gamma,\mathrm{p})}{\sigma^{\mathrm{int}}(\gamma,\mathrm{n})}$ cross-section ratio for ^{58}Ni using the NOVA petawatt laser which is a large-scale low repetition system. The resulting ratio of 3.1(3) agreed with the only previous measurement by Ishkanov *et al* [32]. This experimental effort highlights the potential for the use of high-intensity lasers to determine integral values σ^{int} for a range of charged particle reactions. In the present work, four materials with low to medium atomic number ($12 \leqslant Z \leqslant 42$) were selected. A series of integrated cross-sections $\sigma^{\mathrm{int}}(\gamma, \mathrm{p})$ for stable Mg, Ti, Zn and Mo isotopes were measured and new data with respect to the evolution of the $\frac{\sigma^{\mathrm{int}}(\gamma,\mathrm{n})}{\sigma^{\mathrm{int}}(\gamma,\mathrm{p})}$ ratio with increasing atomic number were derived. The results are in agreement with theoretical calculations which predict a strong influence of the Coulomb barrier in disfavoring proton emission for high Z values and large neutron excess. The new findings contribute towards a better understanding of photo-induced charged particle emission and further the development of theoretical codes such as EMPIRE.

3. Experiment

Since the initial experiments demonstrating the creation of relativistic electrons from the interaction of intense laser fields with matter [33, 34], advances in laser technology have seen a rapid increase with regard to the maximum electron energy. It has been shown that laser acceleration of electrons in gas jets by wakefield acceleration is much more efficient than the acceleration in solid targets, as the interaction length is extended to much higher values (approximately millimetres) via the self-focusing effect [35]. In 2004, Liesfeld *et al* [12] have demonstrated an increase in the reaction yield by a factor of >100 when exchanging the primary solid target with a gas jet [12]. Based on this work, the current study was carried at the Institut für Optik und Quantenelektronik (IOQ) at the University of Jena using the same set-up as depicted in detail in [12]. It is worth pointing out that the introduction of a gas-jet system for the production of electrons is a novelty for laser plasma photon cross-section studies. In the relativistic regime, the resulting electron energy distribution can be described by a quasi-Maxwellian distribution with temperature values kT_{e} of several MeV [17]. Besides the gains with respect to the kT_{e} value and the electron yield, a gas-jet system as the primary electron producer strongly reduces the creation of unwanted particles accelerated to MeV energies from hydrogen and other impurities and surface contaminants as present in experiments using solid conversion targets. The Jena laser system is capable of delivering laser pulses of 80 fs duration with a maximum energy of 1 J and a high repetition rate of 10 Hz. An $f/2$ off-axis parabola focuses the laser pulse with a center wavelength of 800 nm onto a pulsed helium gas-jet target. Further details of the gas-jet system can be found in [16]. In the present work, the laser pulse was adjusted to an energy of 600 mJ, which results in

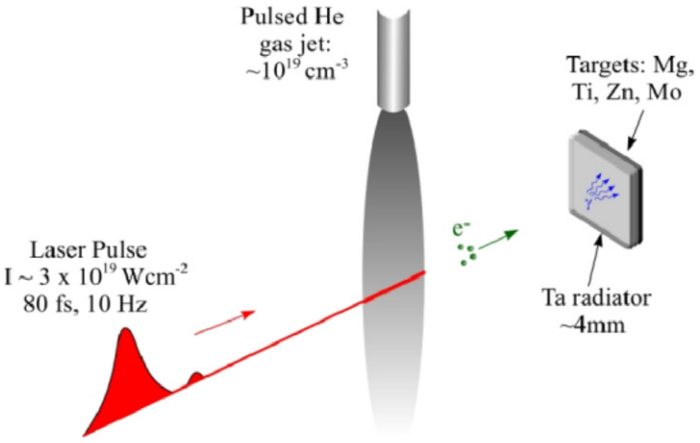

Figure 1. Schematic view of the experimental set-up. The target was placed in direct contact with the tantalum converter to narrowly confine the activated volume.

an intensity $I \sim 3 \times 10^{19}\,\mathrm{W\,cm^{-2}}$ within the measured focal spot diameter of $\sim 5\,\mu$m. The helium gas jet generates a maximum particle density of around $3 \times 10^{19}\,\mathrm{cm^{-3}}$ at a backing pressure of 80 bar within a pulse time of the jet valve of 1 ms. Normal to the nozzle axis, the particle density has a Gaussian profile decreasing exponentially along the axis. It was found that for optimal electron acceleration the laser focus is best positioned close to the maximum gradient of the gas density. The system provides a measured laser contrast ratio of 10^6. In order to convert the forward peaked relativistic electrons emerging from the laser–gas interactions into hard bremsstrahlung photons that can trigger nuclear reactions ($E_\gamma \gtrsim 6$–8 MeV), a 4.1 mm thick tantalum radiator of dimensions $40 \times 40\,\mathrm{mm^2}$ was placed in the vacuum chamber ($p \lesssim 3.5 \times 10^{-2}$ mbar) around 10 cm behind the interaction zone as shown in figure 1. For this specific set-up and identical gas jet pressure and contrast ratio conditions, the beam divergence of the highly energetic electrons was measured to be less than 10 mrad in a previous experiment [12]. This low beam spread results in a very tiny impact area of the relativistic electrons extending to an estimated size of only $\sim 0.8\,\mathrm{mm^2}$ at the front side of the Ta converter. The de-acceleration and bremsstrahlung generation of the impinging highly relativistic electrons ($E_\mathrm{e} > 8$ MeV) within the tantalum radiator were modeled with GEANT4 simulations [36, 37]. The calculations assumed a Boltzmann distribution of electrons exhibiting a temperature value of $kT_\mathrm{e} = 2.9$ MeV (see section 4 for kT_e measurement). The obtained results are coherent with outcomes from similar theoretical work on laser–matter interactions by Galy *et al* [38] and MCNPX calculations [39, 40]. Calculations for the resulting spatial distribution of bremsstrahlung radiation emerging from the rear side of the tantalum converter and the molybdenum target are shown in figure 2. The estimations show that around 70% of the total high-energy photon flux emerging from the back side of the radiator is confined into a narrow cone covering a small area $\lesssim 8\,\mathrm{mm^2}$ (rms value ~ 2.8 mm, see figure 2(a)). This theoretical estimation is in coherence with experimental observations by Schwoerer *et al* [41] using the same laser system.

As indicated in figures 1 and 2(c) the targets, namely MgF_2 and natural Ti, Zn and Mo bulk probes, were directly attached to the tantalum converter. For each radiator/target

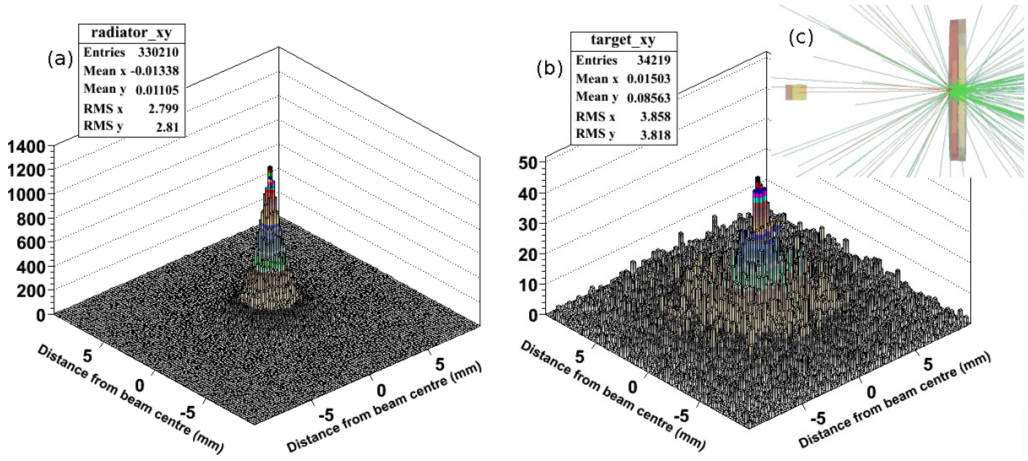

Figure 2. GEANT4 simulation of the spatial distributions of high energetic bremsstrahlung photons induced by relativistic electrons with $E_e > 8\,\mathrm{MeV}$ and $kT_e = 2.9\,\mathrm{MeV}$ at the rear side of the 4.1 mm tantalum radiator (a) and emerging from the rear side of the conjoined 4 mm molybdenum target (b). The rms value for the molybdenum suggests that ∼70% of the total high-energetic γ flux stays within a narrow cone with $\varnothing \lesssim 4\,\mathrm{mm}$ throughout the Mo target. The inset (c) shows the result of a typical GEANT4 simulation and the geometry of the radiator/target arrangement with electron impact from left (radiator in red, Mo target in light brown and calculated traces of bremsstrahlung photons in green and electrons in red color).

combination, GEANT4 simulations were performed in order to estimate the straggling of the bremsstrahlung photons within the target and the transmission of electrons into the target probe. These calculations allowed us to estimate the spatial confinement of photon- and electron-induced reactions. In the experiment, each radiator/target combination was irradiated with around 5000 laser pulses within a time interval (Δt_{irr}) of around 8 min. After irradiation, the targets were removed from the vacuum chamber within a handling time (Δt_{han}) of approximately 5 min and placed at a distance of ∼2.5 cm in a centered position in front of a coaxial Ge detector (Canberra GX3518; diameter: $2\frac{1}{2}$ inches). The detector was equipped with a very thin plastic entrance window in order to maximize the detection of low-energy photons. The single γ-spectra were recorded for well-defined time intervals to obtain half-life information. After correction for the natural occurring background radiation, the measured and identified γ-rays represent a yield measure for their corresponding reaction channels exhibiting half-lives ranging from several minutes to days. Due to the time constraints with respect to the sample handling and the maximal feasible acquisition time, the system was not sensitive to very short-lived $t_{1/2} \ll 5\,\mathrm{min}$ and long-lived $t_{1/2} \gg 1\,\mathrm{day}$ transitions. After calibration, the energies and yields of the measured and background-corrected γ-ray transitions were determined by fitting a Gaussian distribution to the photo-peaks, resulting in energy uncertainties of less than 0.5 keV. The relative efficiency of the detector as a function of the energy $\epsilon_{\mathrm{rel}}(E)$ was determined with a combined ^{133}Ba/^{152}Eu source. Using a mono-energetic ^{137}Cs source the absolute peak efficiency was found to be $\epsilon_{\mathrm{abs}}(661\,\mathrm{keV}) = 7.36(24)\%$. This measurement enabled normalization of all intensities and, hence, absolute yield values N_0 for the production of isotopes could be obtained.

After the energy and efficiency calibration, the half-life of each prominent transition was determined. All γ-ray transitions of interest were unambiguously identified. The raw intensities were adjusted with the known branching ratios (including internal conversion) as published in the NNDC database [27]. Additionally, the intensities were re-normalized with respect to the total acquisition time Δt_{acq} and dead-time effects. The pulsed irradiation of the probe materials and the successive decay of the radionuclides into their daughter isotopes were simulated as well. All intensities were referenced to the activity at t_0, which denotes the end of the laser activation period Δt_{irr}. Furthermore, the intensity loss which occurred during the handling period Δt_{han} was accounted for. For short half-lives $t_{1/2} \lesssim 20$ min this adjustment is important since $t_{1/2} \sim \Delta t_{\mathrm{irr}} + \Delta t_{\mathrm{han}}$. The loss of γ-ray intensity due to self-absorption within the thick target probes (absorption coefficients from [42, 43]) and the target-detector geometry ($\Omega_{\mathrm{det}} = 2.09$ sr) were also taken into consideration with additional GEANT4 simulations. These calculations used the estimated bremsstrahlung and electron distributions within the target probe that were modeled previously with GEANT4 in order to account for the expected spatial distribution of reaction products (see e.g. in figure 2(b) for molybdenum). Finally, after re-normalization with the isotopic abundance in the target, the integral yield of the photo-induced residual radioactive nuclei N_0 present at time t_0 was determined.

4. Results and discussion

4.1. Temperature measurement

4.1.1. Temperature measurement facilitating $^{181}Ta(\gamma, n)^{180}Ta$ and $^{181}Ta(\gamma, 3n)^{178}Ta$. In a first measurement, the yield ratio of the radioactive isotopes ^{180}Ta and ^{178}Ta as produced by photo-nuclear reactions in the Ta radiator was studied in order to derive the temperature of the high-energy bremsstrahlung photons. The feasibility of this and similar photo-nuclear diagnostic methods has been demonstrated previously using various activation targets [12, 14, 17, 31] for kT_{e} values ranging from ~2 to 35 MeV and is described in detail in [44]. At the high relativistic energies ($kT_{\mathrm{e}} > 2$ MeV) as present in this experiment, the quasi-Maxwellian energy distribution [14] can be approximated with a Boltzmann distribution, whereby T_{e} roughly scales with the square root of the laser intensity I [45]. Furthermore, it is known that in the ultra-relativistic regime, the bremsstrahlung photons will have almost the same temperature as the incident hot electrons ($T_\gamma \lesssim T_{\mathrm{e}} = T$) [46, 47]. As photons inducing (γ, n) or (γ, p) reactions in the selected elements must have a minimum energy of $E_\gamma \gtrsim 6$–8 MeV, a Boltzmann-tail distribution is well suited to describe their distribution in the GDR regime:

$$\frac{\mathrm{d}N_\gamma(E)}{\mathrm{d}E} = N_\gamma^0(E)\,\mathrm{e}^{-E/kT}, \tag{2}$$

with N_γ^0 being the amplitude in units of MeV^{-1} and k being the Boltzmann constant. For a specific reaction with an energy-dependent cross-section given by $\sigma(E)$ the number of residual nuclei produced by bremsstrahlung can be derived from the following expression:

$$N = Q_{\mathrm{a}} d \int_{E_{\mathrm{th}}}^{\infty} \sigma(E)\, N_\gamma(E)\, \mathrm{d}E, \tag{3}$$

where Q_{a} is the atomic density of the target, d its thickness and E_{th} the reaction threshold energy. In order to determine the temperature based on the two formulae above, the yield ratio of the unstable reaction products $N_{^{178}\mathrm{Ta}}/N_{^{180}\mathrm{Ta}}$ was firstly determined. As natural

tantalum consists of 99.988% ^{181}Ta, these isotopes can only be created via photon reactions: ^{181}Ta(γ, n)^{180}Ta and ^{181}Ta(γ, 3n)^{178}Ta or the equivalent (e, e′n),(e, e′3n) electrodisintegration channels. Though exhibiting a much lower cross-section ($\sigma_e(E) \ll \sigma_\gamma(E)$), the electron-induced processes cannot simply be disregarded, as one has to consider the yield ratio between electrons and photons (N_e/N_γ) present in the radiator. ^{178}Ta decays via two distinct electron capture (EC) processes from its 1^+ or its 7^- level into ^{178}Hf, while ^{180}Ta transmutes into ^{180}Hf (EC decay) or ^{180}W (β^- decay). Coinciding with these decays are two prominent transitions at 426 keV($^{178}_{73}\mathrm{Ta}_{(7^-)} + e^- \rightarrow {}^{178}_{72}\mathrm{Hf} + \nu_e$) and 103 keV($^{180}_{73}\mathrm{Ta} \rightarrow {}^{180}_{74}\mathrm{W} + e^- + \overline{\nu_e}$). Although there are other intense transitions, these two are specifically chosen as references for the deduction of the yield ratio, as they are free from contaminating contributions of other transitions. In the present work half-lives of 8.48(32) h for the 103 keV transition and 2.68(31) h for the 426 keV transition were obtained, which are in good agreement with the literature values of 8.15 and 2.36 h respectively [27]. A ratio of $N_{^{178}\mathrm{Ta}}/N_{^{180}\mathrm{Ta}} = 3.06(48) \times 10^{-4}$ was obtained. The experimental uncertainty is mainly caused by the efficiency calibration for energies of $E_\gamma < 120$ keV and the inaccuracy for the published branching ratio of the 103 keV transition in the decay of ^{180}Ta of 0.81(23)%. In order to account for the influence of the electrodisintegration, the measurement of $\sigma_e(E)$ on ^{181}Ta of Cataldi *et al* [48] was used, which extends from the threshold energy for neutron emission, $S_n(^{181}\mathrm{Ta}) = 7.6$ MeV, to 22 MeV where σ(e, e′n) has a value of $\sim$2.8 mb (figure 3). As the yield ratio N_e/N_γ could not be derived experimentally, the theoretical calculations of bremsstrahlung production from high-intensity laser matter interactions as described in [38] were considered. Additionally GEANT4 [36, 37] and MCNPX [39] simulations were performed in order to model the photon-to-electron flux conversion efficiencies $\frac{\Phi_\gamma^{\mathrm{out}}}{\Phi_{e^-}^{\mathrm{in}}}$ as a function of the electron energy and the radiator thickness. Based on these calculations and additional studies of the analytic and Monte-Carlo representation of Ta-bremsstrahlung spectra [40, 49], as well as on the estimation $kT_e > 2$ MeV for the Jena laser gas jet system [12], a 23(10)% contribution from electrodisintegration was evaluated for the production of ^{180}Ta in the present work (figure 3). Interestingly, for electron energies between 20 and 35 MeV, older studies by Brown *et al* [52] showed that the photon-to-electron-induced activity (F factor) for $\frac{^{181}\mathrm{Ta}(\gamma,\mathrm{n})^{180}\mathrm{Ta}}{^{181}\mathrm{Ta}(\mathrm{e},\mathrm{e}'\mathrm{n})^{180}\mathrm{Ta}}$ declines smoothly from $\sim$6 to $\sim$5. Extrapolation of the F factor to lower E values, followed by an integration weighted with the modeled N_e distribution, agrees with the present estimate. The contribution of electrodisintegration to the production of ^{178}Ta cannot be deduced from a direct measurement, as the threshold energy for $3n$ emission coincides with the highest electron energy E for which $\sigma_e(E)$ was determined [48]. Therefore, the F factor evaluation depicted in [52], which suggests a slight increase in electrodisintegration for the total activity in tantalum radiators for $E \lesssim 35$ MeV, was taken into consideration. Based on this estimate a 30(10)% contribution of (e, e′3n) towards the production of ^{178}Ta was determined. As the giant quadrupole resonance (GQR) contribution within the GDR regime is small [48], this approximation is justifiable. In order to derive kT for the bremsstrahlung photons the (γ, n) and (γ, 3n) cross-section measurements from [50, 51] were used. Both distributions are depicted in figure 3. Taking into account the influence of the electrodisintegration, a temperature value of $kT = 2.73^{+0.36}_{-0.31}$ MeV was determined based on the measured yield ratio of the tantalum isotopes. The main contributions towards the experimental uncertainty arise from the discussed presence of the (e, e′n), (e, e′3n) reactions and the standard error value of the published intensity value for the 103 keV transition. The uncertainty of the accepted ^{181}Ta(γ, n)^{180}Ta and ^{181}Ta(γ, 3n)^{178}Ta cross-sections added around 20% to the error in the final result.

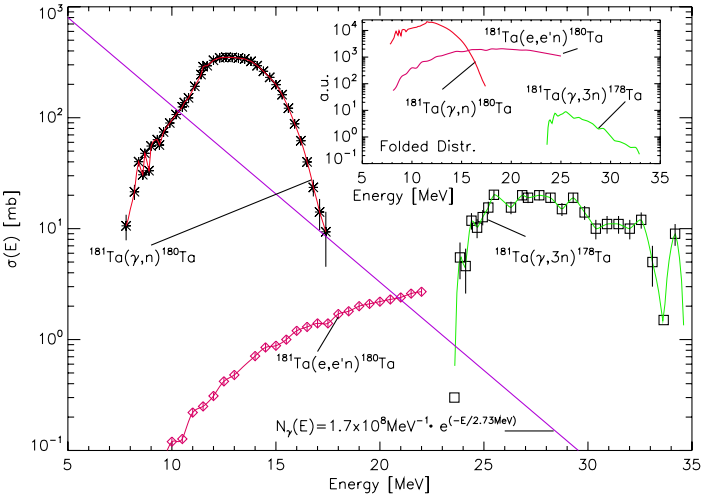

Figure 3. Cross-sections for ^{181}Ta(γ, n)^{180}Ta (red line, ($\star$)), ^{181}Ta(γ, 3n)^{178}Ta (green line, ($\square$)) and ^{181}Ta(e, e′n)^{178}Ta (violet line, ($\diamond$)) according to [48, 50, 51]. The photon distribution $N_\gamma(E)$ is given in arbitrary scale. The value $kT = 2.73$ MeV was derived from matching the ratio of the integrals of the folded ^{181}Ta(γ, n)^{180}Ta and ^{181}Ta(γ, 3n)^{178}Ta distributions to the measured yield ratio, after correction for the contribution of electrodisintegration. The folded distributions representing the integrands of equation (3) are displayed for all three reactions as solid lines in arbitrary units (au) in the inset.

4.1.2. Temperature measurement facilitating $^{12}C(\gamma, n)^{11}C$ and $^{63}Cu(\gamma, n)^{62}Cu$. In addition to the temperature measurement using the tantalum converter, a second independent measurement using a C/Cu stack consisting of a 4 mm thick plastic (CH_2) and a 3.25 mm thick copper foil was also performed. The stack was placed directly behind the Ta converter in the target position. The cross-section distributions for ^{12}C(γ, n)^{11}C and ^{63}Cu(γ, n)^{62}Cu are well known [53, 54] and have been previously used as standards for temperature measurements in laser plasma research [14]. The reaction products ^{11}C and ^{62}Cu both decay via β^+ emission, giving rise to a pair of 511 keV annihilation photons, which were measured with an Na(I) scintillation coincidence counter system. After correcting the measured activities as described before, a ratio of $N_{^{11}C}/N_{^{62}Cu} = 8.58(13) \times 10^{-3}$ was derived. The main uncertainty in this measurement arises from the very low intensity of annihilation γ radiation associated with the decay of ^{11}C, with a decay rate of only $\sim 0.35\,s^{-1}$. Based on calculations with GEANT4 and CASINO [55] and the measurement of ^{12}C(e, e′n)^{11}C by Kline *et al* [56], the electron-induced yield contribution towards the production of ^{11}C was estimated to be less than 8%, as the thick tantalum radiator was placed in front of the C/Cu stack. Thus, it shifts the electron distribution present in the plastic/copper stack $N_e^{C/Cu}(E)$ by 13 MeV towards lower energies compared to the initial distribution $N_e^0(E)$ emerging from laser–gas interaction, cutting off all electrons with an initial energy of less than 13 MeV. As a result, the electron-to-photon intensity ratio at a given energy $N_e^{C/Cu}(E)/N_\gamma^{C/Cu}(E)$ is strongly reduced compared to the corresponding value for the Ta radiator since the high-energy photon distribution does not greatly change due to self-absorption between the converter and the C/Cu-stack. Similar estimations with regard to the ^{62}Cu production from the reaction ^{63}Cu(e, e′n)^{62}Cu [57] lead to a low approximate value of

$\frac{N(^{63}\mathrm{Cu(e,e'n)}^{62}\mathrm{Cu})}{N(^{63}\mathrm{Cu}(\gamma,\mathrm{n})^{62}\mathrm{Cu})} < 0.04$. Based on these results a best fit approach of $kT = 3.09^{+0.23}_{-0.22}$ MeV was derived from the C/Cu-stack data.

4.1.3. Determination of temperature. Adding the two independent measurements in quadrature a final average value of $kT = 2.90(23)$ MeV was adopted. For N_γ^0 a value of $1.7(2) \times 10^8\,\mathrm{MeV}^{-1}$ was obtained. For this calculation, the low-energy part of the photon spectra that exhibits a substantial lower temperature [58] was neglected, as only the high-energy part covering the GDR regime ($E > 7$ MeV) was of interest. The total conversion efficiency of laser light into photon energy was found to be $3.3(4) \times 10^{-4}$, which is in agreement with observations of Behrens *et al* performed at the same laser system [47] and fits approximations derived from measurements of Liesfeld *et al* [12].

4.2. Photonuclear (γ, p) reactions in Mg, Ti, Zn and Mo

Samples of MgF_2 and natural Ti, Zn and Mo were selected and the integral cross-sections $\sigma^{\mathrm{int}}(\gamma, \mathrm{p})$ for ^{25}Mg, ^{48,49}Ti, ^{68}Zn and ^{97,98}Mo were measured for the first time. Covering a wide Z-range between 12 and 42, the present investigation also added information with regard to the evolution of the $\frac{\sigma^{\mathrm{int}}(\gamma,\mathrm{n})}{\sigma^{\mathrm{int}}(\gamma,\mathrm{p})}$ cross-section ratio for light to medium-sized nuclei within the GDR regime. All main reaction channels which produce radioactive isotopes with $t_{1/2} > 300$ s were unambiguously identified, confirming and extending very preliminary results previously reported in [59]. The data were analyzed as discussed in the previous section and the influence of possible competing reactions, leading to the same final nuclei, was estimated. The values for $\sigma^{\mathrm{int}}(\gamma, \mathrm{p})$ were derived from a mean square fit using EMPIRE calculations to reproduce the experimental yield ratios. This methodology is depicted in the work of Magill *et al* [20] for the measurement of $\sigma^{\mathrm{int}}(^{129}\mathrm{I}(\gamma, \mathrm{n})^{128}\mathrm{I})$. In general, the measured intensities found in this work were of high magnitude and allowed a clear determination of a series of integral cross-sections, thus promoting the use of bremsstrahlung radiation of laser-accelerated electrons as a new tool for nuclear studies. The depicted method is competitive with traditional accelerator-based experiments for this purpose. Within this frame set, it is important to point out that a total of three measured integral cross-sections σ^{int} could be determined which allowed a comparison with previously known data. Good agreement was found for all these cases: $\sigma^{\mathrm{int}}(^{67}\mathrm{Zn}(\gamma, \mathrm{p})^{66}\mathrm{Cu}) = 135(58)$ MeV mb (this work) and 118 MeV mb (according to [60]); $\sigma^{\mathrm{int}}(^{64}\mathrm{Zn}(\gamma, 2\mathrm{n})^{62}\mathrm{Zn}) = 76(32)$ MeV mb (this work) and 44 MeV mb (according to [61]) and $\sigma^{\mathrm{int}}(^{70}\mathrm{Zn}(\gamma, \mathrm{n})^{69m_1}Zn) = 200(29)$ MeV mb (this work) and ~140–260 MeV mb (according to estimate from measurements [62] and branching ratios [27]). These results clearly underline the suitability of the chosen experimental approach for the study of photo-proton interaction.

4.2.1. ^{25}Mg. The composite target MgF_2 with natural magnesium consisting of ^{24}Mg (78.99%), ^{25}Mg (10%) and ^{26}Mg (11.01%) was chosen since magnesium has a relatively low Z and the $^{25}\mathrm{Mg}(\gamma, \mathrm{p})^{24}\mathrm{Na}$ reaction with $E_{\mathrm{th}} = 12.06$ MeV had not yet been studied. The final product ^{24}Na decays partially via $^{24}\mathrm{Na} \rightarrow {}^{24}\mathrm{Mg} + \mathrm{e}^- + \overline{\nu_\mathrm{e}}$ emitting two strong γ transitions in the process: 1368 keV (branching $I_\gamma = 100\%$) and 2754 keV ($I_\gamma = 99.94\%$). For the other two stable magnesium isotopes ^{24,26}Mg the (γ, n) and (γ, p) cross-sections have been measured in great detail and $^{25}\mathrm{Mg}(\gamma, \mathrm{p})^{24}\mathrm{Na}$ data complete the evaluation of the $\frac{\sigma^{\mathrm{int}}(\gamma,\mathrm{n})}{\sigma^{\mathrm{int}}(\gamma,\mathrm{p})}$ ratio for stable isotopes with $Z = 12$, as $^{25}\mathrm{Mg}(\gamma, \mathrm{n})^{24}\mathrm{Mg}$ is known [63]. In addition, the

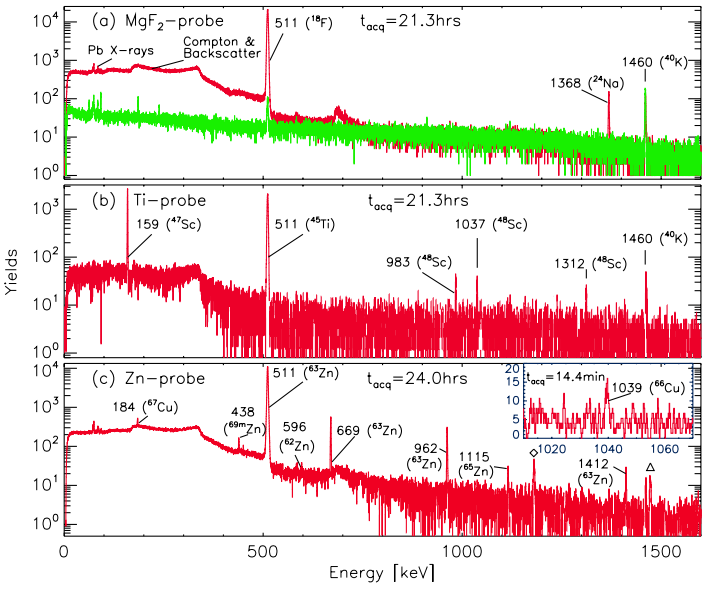

Figure 4. Activation spectra of the MgF_2 (a), Ti (b) and Zn targets (c) derived in this work. Energies of the most prominent transitions are labeled in conjunction with their assigned photo-nuclear reaction product given in brackets. The raw MgF_2 activation spectra are shown in red color in (a) together with the natural background radiation which was measured for the same Δt_{acq} after the MgF_2 target and the Ta radiator were removed (green). The dominating 511 keV annihilation peak results from the β^+ decay of ^{18}F. The background-corrected titanium activation spectra are depicted in (b). The most prominent peak at 159 keV is caused by ^{48}Ti(γ, p)^{47}Sc and the subsequent decay of ^{47}Sc. The three transitions at 983, 1037 and 1312 keV belong to the decay of ^{48}Sc, produced via ^{49}Ti(γ, p)^{48}Sc. The activation spectra for the natural Zn sample ($\Delta t_{\mathrm{acq}} = 24.0$ h) are shown in (c). The intense 511 keV photopeak corresponds to annihilation following the β^+ decay of ^{63}Zn. Summation peaks of the strongest photopeaks are also seen (511 + 669 keV (◊), 511 + 962 keV (△)). The inset in the picture (blue) shows the presence of the 1039 keV transition resulting from the fast decay of ^{66}Cu ($t_{1/2}^{\mathrm{Lit.}} = 5.12$ min) emerging from ^{67}Zn(γ, p)^{66}Cu as observed for $\Delta t_{\mathrm{acq}} =$ 14.40 min. All spectra show the 1460 keV background radiation associated with ^{40}K.

(γ, n) reaction process on ^{19}F provides a reference to derive the reaction yield, as the product ^{18}F decays via β^+ emission. The coincident 511 keV annihilation photons account for a summed branching of 193.46% per decay. In order to maximize the measured yield, a bulk sample of 9 mm thickness and 60 mm diameter was chosen. The measured spectra (red) and the background distribution (green) obtained for $\Delta t_{\mathrm{acq}} = 21.3$ h are given in figure 4(a).

The energy spectra are clearly dominated by the 511 keV photopeak. The 1368 keV photon decay is visible as well as the 1460 keV transition from the ^{40}K background radiation. The 2754 keV transition is just outside the detection energy range. The half-lives for the photopeaks were found to be 1.94(11) h for 511 keV ($t_{1/2}^{\mathrm{Lit.}} = 1.83$ h) and 15.3(8) h for the 1368 keV ($t_{1/2}^{\mathrm{Lit.}} = 14.95$ h) transition. After background subtraction an experimental value of

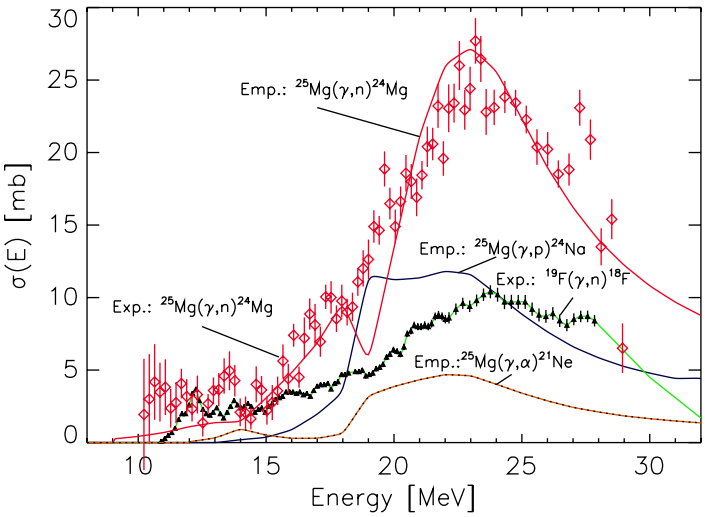

Figure 5. The measured and evaluated cross-sections and uncertainties for ^{25}Mg(γ, n)^{24}Mg ($\Diamond$) and ^{19}F(γ, n)^{18}F ($\triangle$) according to [63, 65]. For $E > 28$ MeV the experimental distributions were extended with the tail of a Lorentzian approximation provided by EMPIRE. The fitted curves derived from EMPIRE calculations are depicted as dotted lines in red for ^{25}Mg(γ, n)^{24}Mg and green for ^{19}F(γ, n)^{18}F. The calculated ^{25}Mg(γ, p)^{24}Na distribution is shown by a blue solid line; the predicted ^{25}Mg(γ, α)^{21}Ne cross-section is shown as a brown solid line with black dots.

$N_{^{18}\mathrm{F}}/N_{^{24}\mathrm{Na}} = 1.90(9)$ was extracted. In order to interpret this result the influences of possible target impurities, electrodisintegration processes and contaminating reactions that could lead to the production of ^{18}F and ^{24}Na were estimated. Impurity levels of Al, Fe and Ti were $<0.01\%$ and their influence could be safely neglected. No direct measurement of the electrodisintegration of ^{25}Mg in the GDR regime exists and an experiment of Dias *et al* [64] in the neighboring ^{29}Si nucleus was examined to evaluate the influence of electron-induced reactions, which was found to be negligibly small, using the same assumptions on N_e/N_γ as for the C/Cu stack data. Similar estimates were derived for ^{18}F. Based on EMPIRE calculations the contaminant ^{26}Mg(γ, np)^{24}Na reaction was estimated to add much less than 3% towards the total intensity of ^{24}Na isotopes. Since all possible contaminant contributions are well within the experimental uncertainty, $N_{^{18}\mathrm{F}}/N_{^{24}\mathrm{Na}} = 1.90(9)$ represents the proportion of the photo-induced processes $\frac{^{19}\mathrm{F}(\gamma,\mathrm{n})^{18}\mathrm{F}}{^{25}\mathrm{Mg}(\gamma,\mathrm{p})^{24}\mathrm{Na}}$. Referring to the known cross-section distribution for $\sigma(E)(^{19}\mathrm{F}(\gamma, \mathrm{n})^{18}\mathrm{F})$ [65] the integral cross-section σ^{int} (^{25}Mg(γ, p)^{24}Na) was derived by employing EMPIRE calculations (figure 5) to reproduce the experimental yield ratio. Finally, a value of $\sigma^{\mathrm{int}}(^{25}\mathrm{Mg}(\gamma, \mathrm{p})^{24}\mathrm{Na}) = 198(79)$ MeV mb is proposed. The main contribution towards the experimental uncertainty arises from the high value of $\Delta kT = 0.46$ MeV. The resulting distributions are shown in figure 5. Since ^{25}Mg exhibits a very strong oblate deformation in its ground state ($\epsilon_2 = 0.373$), two resonance energies at $\sim$18.8 and 23.2 MeV are present. For the ^{19}F(γ, n)^{18}F cross-section, it is worth noting that the low-lying E_1 resonance at ~ 12.2 MeV largely affects the yield, which is given by a folding of $\sigma(E)$ with the relativistic bremsstrahlung spectra as expressed in equation (3). The measured cross-section of $\sigma^{\mathrm{int}}(^{25}\mathrm{Mg}(\gamma, \mathrm{n})^{24}\mathrm{Mg})$ leads to a value of $\sigma^{\mathrm{int}}(^{25}\mathrm{Mg}(\gamma, \mathrm{n})^{24}\mathrm{Mg}) = 245(30)$ MeV mb for energies of up to $E_{\mathrm{int}} = 28.5$ MeV [63].

Table 1. Photo-induced integral cross-sections $\sigma^{\mathrm{int}}(\gamma, \mathrm{n})$ and $\sigma^{\mathrm{int}}(\gamma, \mathrm{p})$ for stable Mg isotopes and for ^{48,49}Ti in comparison to the theoretical values derived from the TRK sum rule and experimental results depicted in [70]. For ^{25}Mg and ^{48}Ti, the integral neutron cross-sections are extended by EMPIRE calculations to $E = 40$ MeV. Note: for titanium the total neutron yield: $\sigma^{\mathrm{int}}(\gamma, \mathrm{sn})$ for ^{48}Ti is referenced [71].

Isotope	$\sigma^{\mathrm{int}}(\gamma, \mathrm{n})_{\mathrm{Mg}}$ or $\sigma^{\mathrm{int}}(\gamma, \mathrm{sn})_{\mathrm{Ti}}$ (MeV mb)	$\sigma^{\mathrm{int}}(\gamma, \mathrm{p})$ (MeV mb)	$\sigma^{\mathrm{int}}(\gamma, \mathrm{n}) + \sigma^{\mathrm{int}}(\gamma, \mathrm{p})$ (MeV mb)	$\sigma^{\mathrm{int}}_{\mathrm{TRK}(E_{\mathrm{int}})}$ (MeV mb)	E_{int} (MeV mb)	Reference
^{24}Mg	51.9^{Exp}	183	234.9	220(30)	28.3	[66]–[68]
^{25}Mg	$248(30)^{\mathrm{Exp}}_{E<28.9\,\mathrm{MeV}}$	198(79)	476(103)	360(40)	∼40	[28, 63], this work
	$30(10)^{\mathrm{Emp}}_{28.9<E<40\,\mathrm{MeV}}$					
^{26}Mg	164^{Exp}	101.3	265.3	232(30)	28.6	[66, 69]
^{48}Ti	$398(24)^{\mathrm{Exp}}_{E<27\,\mathrm{MeV}}$	142(52)	610(61)	607(40)	∼40	[25, 28, 71], this work
	$70(20)^{\mathrm{Emp}}_{27<E<40\,\mathrm{MeV}}$					
^{49}Ti	$510(60)^{\mathrm{Emp}}$	67(24)	577(65)	618(40)	∼40	[25, 28], this work

Extrapolating these measurements with the help of the EMPIRE calculations to 40 MeV (figure 5), a ratio of $\frac{\sigma^{\mathrm{int}}(^{25}\mathrm{Mg}(\gamma,\mathrm{n})^{24}\mathrm{Mg})}{\sigma^{\mathrm{int}}(^{25}\mathrm{Mg}(\gamma,\mathrm{p})^{24}\mathrm{Na})} = 1.5(6)$ for the entire GDR region was estimated. For the neighboring stable magnesium isotopes, the corresponding ratios are 0.24(2) for ^{24}Mg [66]–[68] and 1.62(20) for ^{26}Mg [66, 69]. Neutron emission is suppressed in the α-cluster nucleus ^{24}Mg compared to the emission of charged particles. The results are summarized in table 1, in which the predicted effective values $\sigma^{\mathrm{int}}_{\mathrm{TRK}(E_{\mathrm{int}})}(\gamma, \mathrm{tot})$ for dipole excitations according to the classical Thomas–Reiche–Kuhn (TRK) sum rule [72] are included. In order to derive $\sigma^{\mathrm{int}}_{\mathrm{TRK}(E_{\mathrm{int}})}(\gamma, \mathrm{tot})$ for the magnesium isotopes, the experimental data from Wyckoff *et al* [70] were considered, which suggest the exhaustion of the TRK formula: $\sigma^{\mathrm{int}} \sim 60\frac{NZ}{A}$ MeV mb. Based on this assumption, the (γ, n) and (γ, p) reaction processes in ^{25}Mg exhaust the classical sum rule to within 35%, while the experimental data for ^{24,26}Mg fit the estimations within 15%. The obtained values are within the given uncertainties. The high ratio for $\frac{\sigma^{\mathrm{int}}(^{25}\mathrm{Mg}(\gamma,\mathrm{n})^{24}\mathrm{Mg})}{\sigma^{\mathrm{int}}(^{25}\mathrm{Mg}(\gamma,\mathrm{p})^{24}\mathrm{Na})}$ is expected as the unpaired neutron is weakly bound in ^{25}Mg. In figure 6, the ratio $\frac{\sigma^{\mathrm{int}}(\gamma,\mathrm{n})}{\sigma^{\mathrm{int}}(\gamma,\mathrm{p})}$ is given for the three stable Mg isotopes. Results with regard to the reaction yield of $^{25}\mathrm{Mg}(\gamma, \mathrm{p})^{24}\mathrm{Na}$ as well as for all the other photo-proton yields obtained in this work are summarized in table 2.

4.2.2. ^{48,49}Ti. A 2.7 mm thick foil of natural titanium served as the target and the isotopic abundances are ^{46}Ti (8.9%), ^{47}Ti (7.3%), ^{48}Ti (73.8%), ^{49}Ti (5.5%) and ^{50}Ti (5.4%), all of which produce radioactive daughter nuclei via either (γ, n) or (γ, p) reactions. An evaluation regarding the influence of target impurities and electrodisintegration showed that yields arising

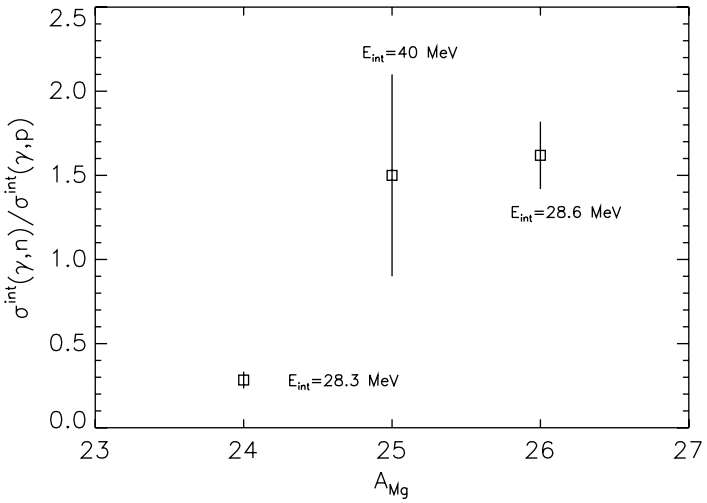

Figure 6. The ratio $\frac{\sigma^{\mathrm{int}}(\gamma,\mathrm{n})}{\sigma^{\mathrm{int}}(\gamma,\mathrm{p})}$ as a function of the mass number A for stable magnesium isotopes. The neutron emission is suppressed in the α-cluster nucleus ^{24}Mg.

from these sources could be neglected (F factor $\gtrsim$8, derived from systematics in [52]). No total photo-absorption cross-section were measured [25, 26] for titanium isotopes and only three (γ, n) or (γ, sn) measurements exist for ^{46,48,50}Ti to date. Figure 4(b) shows the energy spectra after background subtraction obtained after 5000 laser pulses for $\Delta t_{\mathrm{acq}} = 21.2$ h. The spectra are dominated by the 511 keV annihilation photon, as well as by the 159 keV γ-ray, which was attributed to the $^{48}\mathrm{Ti}(\gamma, \mathrm{p})^{47}\mathrm{Sc}$ reaction and its successive decay via β^--emission giving rise to the mixed $M1/E2$ 159 keV transition in ^{47}Ti with a branching ratio of 68.3%. The yield from $^{49}\mathrm{Ti}(\gamma, \mathrm{np})^{47}\mathrm{Sc}$ was estimated to contribute as little as 1–3% to the total measured value, on the grounds of large stoichiometric and threshold energy differences $E_{\mathrm{th}}(^{48}\mathrm{Ti}(\gamma, \mathrm{p})^{47}\mathrm{Sc}) = 11.45$ MeV versus $E_{\mathrm{th}}(^{49}\mathrm{Ti}(\gamma, \mathrm{np})^{47}\mathrm{Sc}) = 19.6$ MeV according to [27]. Similar considerations for the 511 keV photopeak showed that this peak accounts for 98.4(12)% of the $^{46}\mathrm{Ti}(\gamma, \mathrm{n})^{45}\mathrm{Ti}$ reaction, as the contaminant $^{47}\mathrm{Ti}(\gamma, 2\mathrm{n})^{45}\mathrm{Ti}$ has a much higher reaction threshold of $E_{\mathrm{th}}(^{47}\mathrm{Ti}(\gamma, 2\mathrm{n})^{45}\mathrm{Ti}) = 22.72$ MeV and its predicted resonance cross-section $\sigma(E_{\mathrm{res}})$ is only $\sim$2.5 mb [25, 26]. The ^{45}Ti isotope decays via EC into ^{45}Sc, with a half-life of 184.8 min. A $t_{1/2}$ value of 184.8(5) min for the 511 keV photopeak and a $t_{1/2}$ value of 3.36(12) days for the 159 keV transition ($t_{1/2}^{\mathrm{Lit.}} = 3.35$ days) were assigned, thus unambiguously identifying the decays of ^{45}Sc and ^{47}Sc in the irradiated Ti sample. In addition, three low-intensity transitions were found at 983, 1037 and 1312 keV that were assigned to the $^{49}\mathrm{Ti}(\gamma, \mathrm{p})^{48}\mathrm{Sc}$ reaction, as an evaluation of the half-life suggested a similar $t_{1/2}$ for all three transitions, which was greater than 38 h. Furthermore, the intensities matched the branching ratios as depicted in the literature: 983 ($I_\gamma = 101.1\%$), 1037 (97.6%) and 1312 keV (101.1%) validating the present assignment. The sum of all three γ transitions was taken for the investigation. After applying the re-normalization procedure as described in the previous scenario the ratios of $N_{^{45}\mathrm{Ti}}/N_{^{47}\mathrm{Sc}} = 2.96(17)$ and $N_{^{45}\mathrm{Ti}}/N_{^{48}\mathrm{Sc}} = 5.86(31)$ were found (table 2). The integral cross-sections were obtained using the same method as described for the magnesium measurement referring to the $^{46}\mathrm{Ti}(\gamma, \mathrm{n})^{45}\mathrm{Ti}$ measurement of Pywell *et al* [73]. EMPIRE calculations were performed to evaluate the photo-neutron cross-section for ^{48,49}Ti.

Table 2. A summary of the photo-proton reaction yields as observed in this work. The (γ, n) reactions used in the determination of N_0 are referred, as well as the measured and published $t_{1/2}$ values [27].

Target	Reference: (γ, n)	E_γ (keV)	$t_{1/2}$ / $t_{1/2}^{\text{Lit.}}$	Photo-proton: (γ, p)	E_γ (keV)	$t_{1/2}$ / $t_{1/2}^{\text{Lit.}}$	Ratio	Yield N_o
MgF_2	$^{19}F(\gamma, n)^{18}F$	511	1.94(11)/ 1.83 h	$^{25}Mg(\gamma, p)^{24}Na$	1368	15.3(8)/ 14.9 h	$\frac{^{18}F}{^{24}Na} = 1.90(9)$	$^{24}Na \equiv 1.9(2) \times 10^6$
Ti	$^{46}Ti(\gamma, n)^{45}Ti$	511	3.08(7) / 3.08 h	$^{48}Ti(\gamma, p)^{47}Sc$	159	3.36(12)/ 3.35 days	$\frac{^{45}Ti}{^{47}Sc} = 2.96(17)$	$^{47}Sc \equiv 2.3(2) \times 10^6$
Ti	$^{46}Ti(\gamma, n)^{45}Ti$	511	3.08(7)/ 3.08 h	$^{49}Ti(\gamma, p)^{48}Sc$	938 1037 1312	>38(12)/ 43.7 h	$\frac{^{45}Ti}{^{48}Sc} = 5.86(31)$	$^{48}Sc \equiv 3.8(4) \times 10^5$
Zn	$^{64}Zn(\gamma, n)^{63}Zn$	511 596 669 962	37.1(20)/ 38.5 min	$^{67}Zn(\gamma, p)^{66}Cu$	1039	<20(13)/ 5.1 min	$\frac{^{63}Zn}{^{66}Cu} = 4.00(72)$	$^{66}Cu \equiv 1.1(2) \times 10^5$
Zn	$^{64}Zn(\gamma, n)^{63}Zn$	511 596 699 962	37.1(20)/ 38.5 min	$^{68}Zn(\gamma, p)^{67}Cu$	184	60.5(23)/ 61.8 h	$\frac{^{63}Zn}{^{67}Cu} = 5.88(66)$	$^{67}Cu \equiv 5.5(3) \times 10^5$
Mo	$^{100}Mo(\gamma, n)^{99}Mo$	140 181 740	140[a] others: 2.52(55)/ 2.74 days	$^{97}Mo(\gamma, p)^{96}Nb$	778	$\star$[b]/ 23.4 h	$\frac{^{99}Mo}{^{96}Nb} \sim 380(100)$	$^{96}Nb \sim 7.1(36) \times 10^3$
Mo	$^{100}Mo(\gamma, n)^{99}Mo$	140 181 740	140[c]; others: 2.52(55)/ 2.74 days	$^{98}Mo(\gamma, p)^{97}Nb$	657	65(22)/ 72.1 min	$\frac{^{99}Mo}{^{97}Nb} = 123(15)$	$^{97}Nb \equiv 3.0(6) \times 10^4$

[a] Fits the rate equation.
[b] Indeterminate due to low yield.
[c] Fits the rate equation.

In the case of ^{48}Ti, this calculation was benchmarked on experimental results obtained for the total photo-neutron yield $^{48}Ti(\gamma, sn)$ by Sutton *et al* [71]. Optimizing E_{res}, Γ_{res} and σ_{res}, EMPIRE calculations for $^{49}Ti(\gamma, n)^{48}Ti$ lead to similar results compared to that derived from GNASH calculations in [25]. Based on the experimental findings and these calculations, the following σ^{int} values for the GDR regime: $\sigma^{int}(^{48}Ti(\gamma, p)^{47}Sc) = 142(52)$ MeV mb and $\sigma^{int}(^{49}Ti(\gamma, p)^{48}Sc) = 67(24)$ MeV mb are finally proposed (table 3). The latter value includes a $\sim$10(4)% adjustment for the contamination caused by the $^{50}Ti(\gamma, np)^{48}Sc$ reaction with a 3 MeV higher threshold energy than the resonance energy $E_{res} = 19.5$ MeV for $^{49}Ti(\gamma, p)^{48}Sc$. As no (γ, n) measurement is available for ^{49}Ti this value relies heavily on the calculations. The results are consistent with the TRK sum rule: $\sigma^{int}_{TRK(E_{int})}(\gamma, tot)$, thus validating the present method and the EMPIRE calculations (see table 1). It is worth noting that the (γ, n) distribution for ^{48}Ti is predicted to be $\sim$30% broader than for ^{49}Ti, for which the calculation gives $\sigma_{res} \sim 85$ mb. With reference to the measured $\sigma(E)\,dE$ distribution of the total photo-neutron yield $^{48}Ti(\gamma, sn)$ [71], the ratio $\frac{\sigma^{int}(^{48}Ti(\gamma,n)^{47}Ti)}{\sigma^{int}(^{48}Ti(\gamma,p)^{47}Sc)} = 2.4(9)$ is proposed after adjusting the measured data for the effect of $\geqslant$2n emission. Based on EMPIRE, the value for the odd-n ^{49}Ti was estimated to exceed 6.7(2.8) (calculation: $\sigma^{int}(\gamma, n) \sim 450(50)$ MeV mb). It can be concluded that the ratio $\frac{\sigma^{int}(\gamma,n)}{\sigma^{int}(\gamma,p)}$ may vary considerably with increasing neutron excess in titanium isotopes.

Table 3. Measured $\sigma^{\mathrm{int}}(\gamma, \mathrm{p})$ and the corresponding $\frac{\sigma^{\mathrm{int}}(\gamma,\mathrm{n})}{\sigma^{\mathrm{int}}(\gamma,\mathrm{p})}$ ratios valid in the GDR regime for the Mg, Ti, Zn and Mo isotopes surveyed in this work. Parameters E_{res} and σ_{res} are according to equation (1). For ^{25}Mg, the value of FWHM derives from: $\mathrm{FWHM} \sim \sqrt{\Gamma^2_{\mathrm{res}(1)} + \Gamma^2_{\mathrm{res}(2)}}$. For all other isotopes: $\mathrm{FWHM} \sim \Gamma_{\mathrm{res}}$. The threshold energies E_{th} are taken from [26].

(γ, p)	σ^{int} (MeV mb)	$\frac{\sigma^{\mathrm{int}}(\gamma,\mathrm{n})}{\sigma^{\mathrm{int}}(\gamma,\mathrm{p})}$	E_{res} (MeV)	FWHM (MeV)	σ_{res} (mb)	E_{th} (MeV)	Remarks
^{25}Mg$(\gamma, \mathrm{p})^{24}$Na	198(79)	1.5(6)	18.8 23.2	∼14.0	∼11.5 ∼11.9	12.0	Two resonances; $\sigma(\gamma, 1\mathrm{n})$, $\sigma(\gamma, 2\mathrm{n})$, $\sigma(\gamma, \mathrm{sn})$, $\sigma(\gamma, \mathrm{xn})$ measured [63]
^{48}Ti$(\gamma, \mathrm{p})^{47}$Sc	142(52)	2.4(9)	19.5	∼7.8	∼20.0	11.4	$\sigma(\gamma, \mathrm{sn})$ measured [71]
^{49}Ti$(\gamma, \mathrm{p})^{48}$Sc	67(24)	6.7(28)	19.5	∼6.2	∼11.5	11.4	No (γ, n) measurements [25, 26]
^{67}Zn$(\gamma, \mathrm{p})^{66}$Cu	135(58)	5.9(24)	18.5	∼7.8	∼18.9	8.9	$\sigma(\gamma, 1\mathrm{n})$ measured [62]
^{68}Zn$(\gamma, \mathrm{p})^{67}$Cu	169(67)	4.6(18)	21.8	∼8.3	∼18.5	10.0	$\sigma(\gamma, 1\mathrm{n})$ measured [62]
^{97}Mo$(\gamma, \mathrm{p})^{96}$Nb	<50	∼12–30	21.0	∼7.2	∼2.5	9.2	No (γ, n) measurements [25, 26], σ^{int} approximate due to low yield
^{98}Mo$(\gamma, \mathrm{p})^{97}$Nb	115(42)	8.9(34)	23.4	∼7.0	∼16.4	9.8	$\sigma(\gamma, 1\mathrm{n}x)$, $\sigma(\gamma, 2\mathrm{n}x)$, $\sigma(\gamma, 3\mathrm{n})x$, $\sigma(\gamma, 3\mathrm{n}x)$, $\sigma(\gamma, x\mathrm{n})$ and $\sigma(\gamma, \mathrm{sn})$ measured [77]

4.2.3. ^{67,68}Zn. In the investigation of (γ, p) reactions on zinc ($Z = 30$), a stacked target of four 1 mm thick foils of natural zinc was used including five stable isotopes: ^{64}Zn (48.63%), ^{66}Zn (27.90%), ^{67}Zn (4.10%), ^{68}Zn (18.75%) and ^{70}Zn (0.62%). Figure 4(c) shows the activation spectra after background subtraction for a total of 4900 laser pulses and $\Delta t_{\mathrm{acq}} = 24.1$ h. The spectra are dominated by the 511 keV annihilation photon, which was assigned to the EC decay of ^{63}Zn ($t^{\mathrm{Lit.}}_{1/2} = 38.47$ min) resulting from ^{64}Zn$(\gamma, n)^{63}$Zn. As this reaction has been well studied [61, 62, 74], its intensity N_{511} was used to derive the yield ratios. The intruding intensity contribution from the β^+-emitter ^{62}Cu ($t^{\mathrm{Lit.}}_{1/2} = 9.57$ min) emerging out of ^{64}Zn$(\gamma, \mathrm{np})^{62}$Cu was found to contribute as little as 0.5–1.5% of the total N_{511} yield. This evaluation includes intensity loss during the activation period and the handling time ($\Delta t_{\mathrm{irr}} + \Delta t_{\mathrm{han}} = 790$ s), utilizing the measured cross-section by Cook *et al* [75]. The second and third most intense transitions at 669 and 962 keV also arise from the decay of ^{63}Zn (figure 4(c)). Two distinct transitions were found which proved the occurrence of (γ, p) reactions within the Zn sample: 184 keV ($t_{1/2} = 60.5(23)$ h) resulting from ^{68}Zn$(\gamma, \mathrm{p})^{67}$Cu and a weak 1039 keV transition with an estimated half-life of $t_{1/2} < 20$ min which was assigned to the reaction ^{67}Zn$(\gamma, \mathrm{p})^{66}$Cu (see the blue boxed inset in figure 4(c)). The influence of $(\mathrm{e}, \mathrm{e}'\mathrm{n})$ or $(\mathrm{e}, \mathrm{e}'\mathrm{p})$ reactions can be neglected [52, 76]. Target impurities were disregarded on the grounds of their low abundances <0.05%.

Ratios of $N_{^{63}\mathrm{Zn}}/N_{^{67}\mathrm{Cu}} = 5.88(69)$ and $N_{^{63}\mathrm{Zn}}/N_{^{66}\mathrm{Cu}} = 4.00(72)$ were derived. The latter value is corrected with regard to an assumed ∼15(5)% contribution towards the production of ^{66}Cu via the contaminating ^{68}Zn$(\gamma, \mathrm{np})^{66}$Cu reaction. In conjunction with EMPIRE calculations and the known data for ^{64}Zn$(\gamma, \mathrm{n})^{63}$Zn, the following integral cross-sections within the GDR regime were derived: $\sigma^{\mathrm{int}}(^{68}\mathrm{Zn}(\gamma, \mathrm{p})^{67}\mathrm{Cu}) = 169(67)$ MeV mb and $\sigma^{\mathrm{int}}(^{67}\mathrm{Zn}(\gamma, \mathrm{p})^{66}\mathrm{Cu}) = 135(58)$ MeV mb. The value for $\sigma^{\mathrm{int}}(^{67}\mathrm{Zn}(\gamma, \mathrm{p})^{66}\mathrm{Cu})$ corroborates the early result of Ivanchenko *et al* [60] of 118 MeV mb. As the corresponding $\sigma(\gamma, \mathrm{n})$ cross-sections are

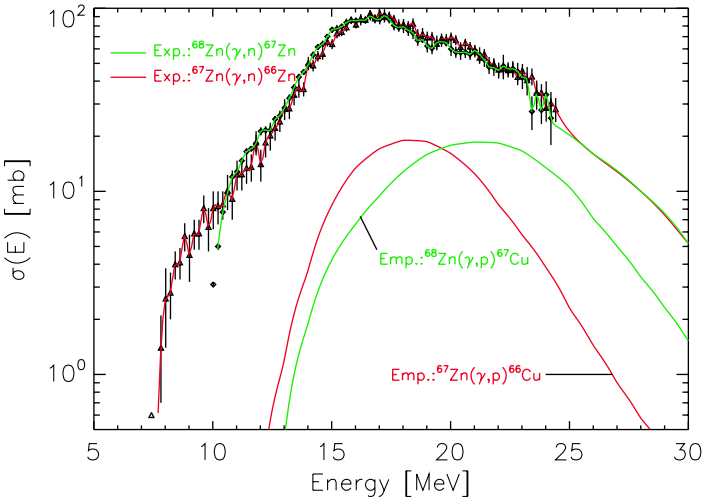

Figure 7. The measured $\sigma(E)$ distributions for the (γ, n) reactions on ^{67}Zn (red dotted line, ($\triangle$)) and ^{68}Zn (green dotted line, ($\Diamond$)) according to [62]. The EMPIRE calculations for the associated (γ, p) reactions are given as solid lines.

known [62], the following ratios based on the present measurements and the EMPIRE calculations are proposed: $\frac{\sigma^{\mathrm{int}}(^{68}\mathrm{Zn}(\gamma,\mathrm{n})^{67}\mathrm{Zn})}{\sigma^{\mathrm{int}}(^{68}\mathrm{Zn}(\gamma,\mathrm{p})^{67}\mathrm{Cu})} = 4.6(18)$ and $\frac{\sigma^{\mathrm{int}}(^{67}\mathrm{Zn}(\gamma,\mathrm{n})^{66}\mathrm{Zn})}{\sigma^{\mathrm{int}}(^{67}\mathrm{Zn}(\gamma,\mathrm{p})^{66}\mathrm{Cu})} = 5.9(24)$. The experimental (γ, n) as well as the proposed (γ, p) cross-sections are depicted in figure 7.

It is worth noting that the evaluation regarding ^{68}Zn$(\gamma, \mathrm{p})^{67}$Zn is in good agreement with predictions based on the GNASH code implemented by the KAERI (Korean Atomic Energy Research Institute) group and published in [26]. There is, however, a discrepancy with regard to the predicted value of E_{res} for the photo-proton decay of ^{67}Zn, which peaks $\sim$3 MeV lower in the present calculations compared to GNASH. The derived integral cross-sections of the (γ, n) and (γ, p) reactions are essentially identical: 930(115) MeV mb for ^{67}Zn and 935(121) MeV mb for ^{68}Zn for $E_{\mathrm{int}} = 35$ MeV. For $Z = 30$ Wyckhoff *et al* [70] predict an integral cross-section of $\sigma^{\mathrm{int}}_{\mathrm{TRK}(E_{\mathrm{int}})} = 1.25(10) \times 60\frac{NZ}{A} \sim 1260$ MeV mb at the given E_{int}. The shortfall of around 330 MeV mb in the sum of $\sigma^{\mathrm{int}}(\gamma, \mathrm{n})$ and $\sigma^{\mathrm{int}}(\gamma, \mathrm{p})$ can be attributed to the onset of 2n emission. The relatively high ratios $\frac{\sigma^{\mathrm{int}}(\gamma,\mathrm{n})}{\sigma^{\mathrm{int}}(\gamma,\mathrm{p})}$ for both neutron-rich zinc isotopes indicate that for $Z \sim 30$ the effect of the Coulomb barrier in disfavoring (γ, p) reactions is already pronounced.

Interestingly, there were two more reaction channels that could be clearly identified. The onset of the ^{64}Zn$(\gamma, 2\mathrm{n})^{62}$Zn reaction is deduced from the presence of a γ-ray at 596 keV and the population of the lowest-lying isomeric level in ^{69}Zn via the reaction ^{70}Zn$(\gamma, \mathrm{n})^{69m_1}$Zn is clearly evident from the 438 keV transition with $t_{1/2} = 15.2(12)$ h ($t^{\mathrm{Lit.}}_{1/2} = 13.76$ h) in the spectra (figure 4(c)). Both reactions proved to be of importance as the measured σ^{int} values could be compared to results from previous experiments, thus supporting the quantitative validity of the present activation measurements and the incorporation of EMPIRE calculations. For $\sigma^{\mathrm{int}}(^{64}\mathrm{Zn}(\gamma, 2\mathrm{n})^{62}\mathrm{Zn})$, a value of 76(32) MeV mb was obtained, which agrees with a previous result from Carlos *et al* [61] of 44 MeV mb. For the isomeric $\frac{9}{2}^+$ level in ^{69m_1}Zn, a value of $\sigma^{\mathrm{int}} = 200(29)$ MeV mb was found, which is $\sim$24(4)% of the overall cross-section for ^{70}Zn$(\gamma, \mathrm{n})^{69}$Zn [27, 62] in fair agreement with the expectations.

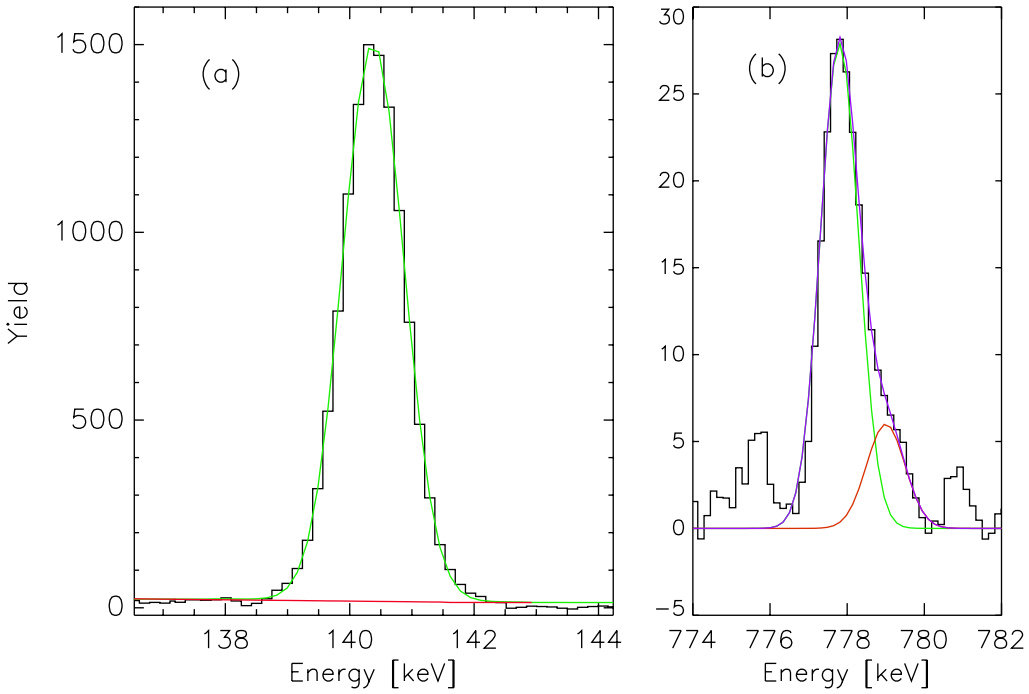

Figure 8. The 140 keV (a) and 778 keV (b) transitions in the molybdenum activation spectra. The 140 keV photopeak was assigned to the decay of ^{99}Mo into ^{99m}Tc. The 778 keV peak clearly shows a shoulder at the higher energetic end, giving evidence of the decay of ^{96}Nb. The Gaussian fit for the 777.9 keV transition emerging from $^{99}\mathrm{Mo} + \beta^- \rightarrow {}^{99}\mathrm{Tc} + \nu_e$ is displayed in green. Based on a best value fit for the contribution of the 778.3 keV transition (red line in (b)), a total yield of $N_{778.3} \sim 45(15)$ is assumed. The convolution of both distributions (blue line in (b)) fits the measurement well.

4.2.4. ^{97,98}Mo. Molybdenum had the highest Z value of 42 of all chosen target materials. The target stack consisted of four 1 mm thick sheets and natural molybdenum has six stable isotopes $^{92,94-98}$Mo plus the quasi-stable ^{100}Mo (abundance: 9.63%) which decays via double-β^-emission with $t_{1/2}^{\mathrm{Lit.}} = 7.8 \times 10^{18}$ years. The measured activation spectra reflects this isotopic variety as a large number of different reactions were initialized. At present, no experiments have been performed to obtain $\sigma(\gamma, \mathrm{tot})$ for any molybdenum isotope [26]. As the purity of the molybdenum target was very high, the possibility of contaminants was excluded. Furthermore, electrodisintegration could be neglected based on the estimates regarding the small flux of electrons transmitted through the thick Ta-radiator. Figure 8(a) shows the most prominent γ transition at 140.5 keV after Δt_{acq}= 1.77 days. This photopeak results from the reaction $^{100}\mathrm{Mo}(\gamma, \mathrm{n})^{99}\mathrm{Mo}$ and the successive decay of ^{99}Mo ($t_{1/2}^{\mathrm{Lit.}}(^{99}\mathrm{Mo}) =$ 2.74 days) into ^{99}Tc. As part of this transmutation is via the 142.7 keV isomeric state ^{99m_1}Tc with $t_{1/2}^{\mathrm{Lit.}}(^{99m_1}\mathrm{Tc}) = 6.01$ h, the 140.5 keV mixed $M1/E2$ transition ($\frac{7^+}{2} \rightarrow \frac{9^+}{2}$) into $^{99}\mathrm{Tc}_{(\mathrm{g.s.})}$, which is populated by this isomer, showed a growth of yield determined by the rate equation: $N_{140} = \frac{\lambda_{^{99}\mathrm{Mo}}}{\lambda_{^{99}\mathrm{Mo}} - \lambda_{^{99m_1}\mathrm{Tc}}}(\mathrm{e}^{-\lambda_{^{99}\mathrm{Mo}}t} - \mathrm{e}^{-\lambda_{^{99m_1}\mathrm{Tc}}t})$ and the activity peaked at $\sim$18(3) h. Three other strong transitions at 181, 740 and (parts of) 778 keV were assigned to the decay

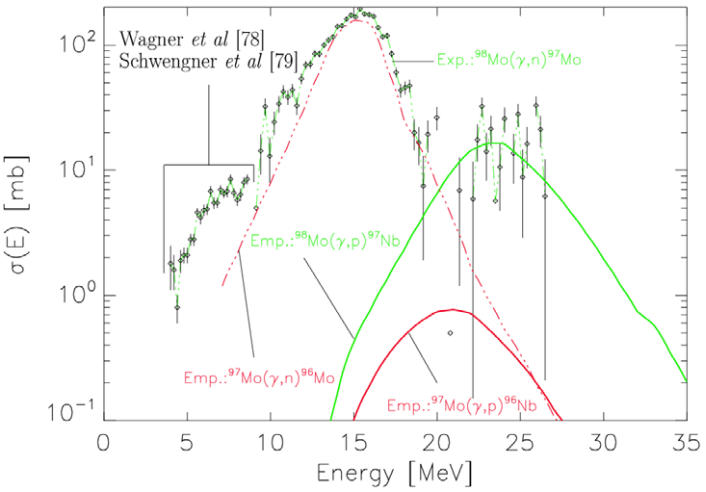

Figure 9. Experimental and calculated $\sigma(E)$ for ^{97,98}Mo(γ, n) and ^{97,98}Mo(γ, p). The cross-section for ^{98}Mo(γ, n)^{97}Nb has been measured (green dotted line, (◇)) [77]–[79]. As no data for ^{97}Mo(γ, n)^{96}Nb exist, $\sigma(E)$ was calculated with EMPIRE using known GDR parameters of ^{98}Mo (red dotted line). The evaluated (γ, p) distributions are shown by thick full lines. Note: the overlap of the calculated ^{98}Mo(γ, p)^{97}Nb with the high-energy tail of the measured ^{98}Mo(γ, n)^{97}Mo cross-section around $E \sim 25$ MeV is purely coincidental.

of ^{99}Mo into ^{99}Tc$_{(g.s.)}$, as their yields rise according to $N(t) = N_0(1 - e^{-\lambda_{^{99}Mo}t})$. The strong 511 keV photopeak emerges solely out of the ^{92}Mo(γ, n)^{91}Mo reaction as is evident from the retrieved half-life of $t_{1/2} = 16.8(11)$ min. No other target isotope can lead to the same reaction product as ^{93}Mo is unstable and a sizeable contribution from $\geqslant$3n channels can be excluded at the given kT. The γ transition at 657 keV belongs to ^{98}Mo(γ, p)^{97}Nb. Its measured half-life of 65(22) min agrees with the given literature value of 72.1 min. The onset of ^{97}Mo(γ, p)^{96}Nb was identified, as the 777.9 keV transition emerging from ^{99}Mo + $\beta^- \rightarrow$ ^{99}Tc + ν_e could not account for all of the 778 keV yield. After adjusting for the relative efficiency and the decay, the clearly skewed line shape and large width of the measured γ transition was attributed to a ~25(10)% contribution from ^{97}Mo(γ, p)^{96}Nb and the successive decay of ^{96}Nb through the 778.3 keV transition with $I_\gamma = 96.45\%$ (see figure 8(b)). A rough estimate for σ^{int} of ^{97}Mo(γ, p)^{96}Nb was derived and the ratios of $N_{^{99}\text{Mo}}/N_{^{97}\text{Nb}} = 123(15)$ and $N_{^{99}\text{Mo}}/N_{^{96}\text{Nb}} \sim 380(100)$ were evaluated. The second value is corrected with regard to an assumed ~15% contribution towards the population of ^{96}Nb via the ^{98}Mo(γ, np)^{96}Nb reaction. Using EMPIRE calculations and the published cross-section of ^{100}Mo(γ, n)^{99}Mo [77] which was recently extended into the low-energy range by Wagner *et al* [78, 79], values of $\sigma^{\text{int}}(^{98}\text{Mo}(\gamma, \text{p})^{97}\text{Nb}) = 115(42)$ MeV mb and $\sigma^{\text{int}}(^{97}\text{Mo}(\gamma, \text{p})^{96}\text{Nb}) \ll 50$ MeV mb were found. Since $\sigma^{\text{int}}(^{98}\text{Mo}(\gamma, \text{n})^{97}\text{Mo}) = 940(50)$ MeV mb for $E_{\text{int}} = 26.8$ MeV [77], a ratio of $\frac{\sigma^{\text{int}}(^{98}\text{Mo}(\gamma,\text{n})^{97}\text{Mo})}{\sigma^{\text{int}}(^{98}\text{Mo}(\gamma,\text{p})^{97}\text{Nb})} \sim 8.9(34)$ is proposed, after extending the measured (γ, n) cross-section with the help of EMPIRE calculations to $E_{\text{int}} = 35$ MeV. Taking into account the experimental value for $\sigma^{\text{int}}(\gamma, \text{sn})$ obtained by Beil *et al* [77], the sum of $\sigma^{\text{int}}(\sigma, \text{sn})$ and $\sigma^{\text{int}}(\sigma, \text{p})$ is estimated to be 1725(74) MeV mb, which should represent $\sigma(\gamma, \text{tot})$ in good approximation. According to [70], a value of $\sigma^{\text{int}}_{\text{TRK}(E_{\text{int}}=35\,\text{MeV})}(\gamma, \text{tot}) = 1.40(15) \times 60\frac{NZ}{A} = 2016(216)$ MeV mb

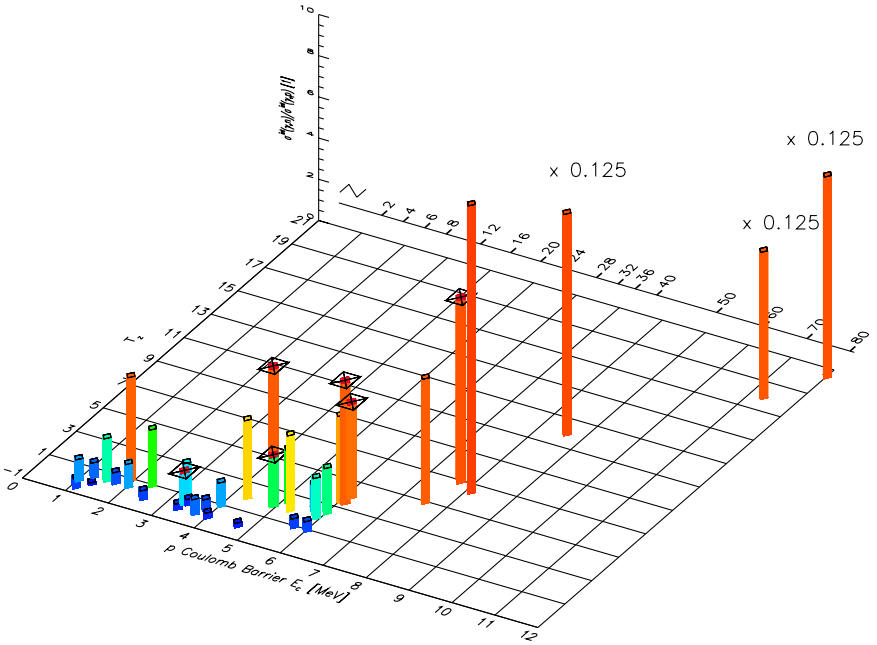

Figure 10. A summary of the published $\frac{\sigma^{\mathrm{int}}(\gamma,\mathrm{n})}{\sigma^{\mathrm{int}}(\gamma,\mathrm{p})}$ ratios as retrieved from the atlas of giant dipole resonances compiled by Varlamov *et al* [26] including the six new ratios as provided by this work (⊠). The x-abscissa is the Coulomb barrier for protons as given in [80]. The y-coordinate represents the isospin projection T_z. The abscissa showing the atomic number Z is to guide the eye. The heat color code was chosen to pronounce the high ratio values among the 37 isotopes on display. The three highest values for ^{124}Sn, ^{184}W and ^{201}Hg are suppressed by 1/8.

is expected, which agrees, within the given uncertainties, with the present estimate as one should include the (γ,α) contribution towards $\sigma(\gamma,\mathrm{tot})$. Since no (γ,n) measurement for ^{97}Mo exists, an estimate of: $12 < \frac{\sigma^{\mathrm{int}}(^{97}\mathrm{Mo}(\gamma,\mathrm{n})^{96}\mathrm{Mo})}{\sigma^{\mathrm{int}}(^{97}\mathrm{Mo}(\gamma,\mathrm{p})^{96}\mathrm{Nb})} < 30$ is proposed based on the approximated reaction yield and EMPIRE. The cross-sections are displayed in figure 9: ^{98}Mo$(\gamma,\mathrm{n})^{97}$Mo from [77] including most recent data from [78, 79] and the EMPIRE evaluations for ^{98}Mo$(\gamma,\mathrm{p})^{97}$Nb, ^{97}Mo$(\gamma,\mathrm{n})^{96}$Mo and ^{97}Mo$(\gamma,\mathrm{n})^{96}$Mo. The EMPIRE calculations for ^{97}Mo$(\gamma,\mathrm{n})^{96}$Mo are almost identical to the GNASH outputs published [26]. In this case, EMPIRE as well as GNASH adopt the GDR parameters from the neighboring ^{98}Mo as shown in figure 9. In line with the expectations, the $\sigma^{\mathrm{int}}(\gamma,\mathrm{n})/\sigma^{\mathrm{int}}(\gamma,\mathrm{p})$ ratios for molybdenum nuclei have the highest values within this study covering $Z = 12$–42. The high ratios manifest the growing influence of the Coulomb barrier and the neutron excess in disfavoring proton emission with rising atomic number.

4.2.5. Measured $\frac{\sigma^{\mathrm{int}}(\gamma,\mathrm{n})}{\sigma^{\mathrm{int}}(\gamma,\mathrm{p})}$ *ratios.* A summary of the $\frac{\sigma^{\mathrm{int}}(\gamma,\mathrm{n})}{\sigma^{\mathrm{int}}(\gamma,\mathrm{p})}$ ratios derived from the present study is shown in table 3 and displayed in figure 10. In addition to the six new values from this work, a survey of all other photo-induced proton-to-neutron ratios currently (March 2008) retrievable from the leading databases [26, 27] is given in figure 10.

Bibliography compilation and the evaluation of relevant experimental data collected over the last four decades are still ongoing, and ∼30% of published work has been scrutinized and is

included in the latest edition [26]. Figure 10 clearly indicates the suitability and efficiency of the method in delivering crucial data for previously unknown photo-proton reactions and the need for further experimental work, since the overall number of published $\frac{\sigma^{\mathrm{int}}(\gamma,\mathrm{n})}{\sigma^{\mathrm{int}}(\gamma,\mathrm{p})}$ ratios is indeed very low (<40). All ratios measured in this work are in line with the expectations and they fit well into the systematic behavior exhibited by other isotopes. The new data from this work contribute towards a better understanding of the growth of $\frac{\sigma^{\mathrm{int}}(\gamma,\mathrm{n})}{\sigma^{\mathrm{int}}(\gamma,\mathrm{p})}$ with increasing atomic number and as a function of neutron excess. The increase in the measured ratios with Z is obviously caused by the increase in the Coulomb barrier (from [80]) which favors (γ, n) over (γ, p) emission. The measurements on zinc and molybdenum suggest a slight enhancement of $\frac{\sigma^{\mathrm{int}}(\gamma,\mathrm{n})}{\sigma^{\mathrm{int}}(\gamma,\mathrm{p})}$ in the odd n systems compared to their more tightly bound even-n neighbors.

5. Summary

The present investigation is the most comprehensive study of photo-proton reactions driven by bremsstrahlung radiation of laser-accelerated electrons to date. It clearly demonstrates the suitability of high-power laser research to contribute substantial new information to the study of nuclear physics. In total, six new values for $\sigma^{\mathrm{int}}(\gamma, \mathrm{p})$ processes and $\frac{\sigma^{\mathrm{int}}(\gamma,\mathrm{n})}{\sigma^{\mathrm{int}}(\gamma,\mathrm{p})}$ ratios for isotopes with $Z = 12$–42 are proposed, thus extending known datasets by a significant amount. The depicted activation method is a useful tool for nuclear investigations and its merits and limits are known to the present team. It was demonstrated that laser-induced bremsstrahlung radiation triggered nuclear reactions with thresholds above 10 MeV, and integral activation yields could be determined in offline γ analysis with reasonably good accuracy. A complication arises from the fact that in each case the influence of electrodisintegration had to be evaluated, since there is no rejection of electrons in the set-up. It has been shown that the use of a thick radiator reduced the contribution by $(\mathrm{e}, \mathrm{e}'x\mathrm{n})$ and $(\mathrm{e}, \mathrm{e}'x\mathrm{p})$ and that photo-induced reactions were predominant. Furthermore, since the very narrow spatial distribution of the relativistic electrons creates a small well-defined activation volume, a simulation of the experimental condition with highest precision is possible. The good spatial confinement facilitates the evaluation of γ self-absorption in the thick samples. The derivation of σ^{int} for photo-proton emission relies on the theoretical predictions of the GDR parameters E_{res}, Γ_{res} and σ_{res}. Based on concepts established by the works of Stoyer *et al* and Magill *et al*, this work referred to state-of-the-art EMPIRE calculations to obtain maximum alignment between the accurately measured yield ratios and the theoretically predicted distribution of $\sigma(E)\,\mathrm{d}E$. This empirical procedure leads to the proposed values for σ^{int} within the GDR-dominated regime. It was proved that without exception the $\sigma^{\mathrm{int}}(\gamma, \mathrm{p})$ and $\sigma^{\mathrm{int}}(\gamma, \mathrm{n})$ results agreed with the TRK-dipole sum rule within the margins of uncertainty. Moreover, the comparison with existing data showed good agreement for all the three cases where reference data were obtainable e.g. for $\sigma^{\mathrm{int}}(^{67}\mathrm{Zn}(\gamma, \mathrm{p})^{66}\mathrm{Cu})$. The EMPIRE calculations performed in this work agreed rather well with published data based on the GNASH code [25, 26]. The obtained $\frac{\sigma^{\mathrm{int}}(\gamma,\mathrm{n})}{\sigma^{\mathrm{int}}(\gamma,\mathrm{p})}$ ratios for the light to medium heavy targets showed the increasing influence of the Coulomb barrier in inhibiting proton emission with growing Z values. For light systems, proton emission exhibits cross-sections comparable to those for (γ, n) reactions, as seen in ^{25}Mg. The ratio increased rapidly from ^{24}Mg to ^{25}Mg, but did not further increase between ^{25}Mg and ^{26}Mg. For growing Z values, the influence of the Coulomb-barrier dominates besides an increase in neutron excess. It could be shown that the integral cross-section for neutron emission in the examined ^{97,98}Mo isotopes is more than eight times that of the corresponding

values for proton emission. It is expected that this work will stimulate more laser-based photo-proton studies. A very natural first extension of the current work would be the investigation of photonuclear reactions for elements with Z values in between molybdenum and samarium. Within this region, a series of proton and neutron evaporation channels exist that can be easily studied via the depicted method. As highlighted by Wagner *et al* [81], the origin of a series of neutron-deficient isotopes within $Z = 42$–62 remains mysterious as they are bypassed by the neutron capture process. Experimental data are needed to shed light on the nuclear processes producing such isotopes under astrophysical conditions. Technical improvements for future measurements will be easily achievable by e.g. the use of mono-isotopic targets where available, the rejection of the bremsstrahlung electrons that emerge out of the radiator, a fast target transport mechanism and the use of a multidetector germanium system to optimize detection efficiency. Furthermore, the facilitation of new accelerator sites like the commissioned high-power laser extension to the ELBE linear accelerator at the FZD, Rossendorf, Germany is envisaged. Such conjoined accelerator systems will allow a direct comparison between laser and traditional electron accelerator-based studies. Besides new insights into photo-induced reactions at stellar temperatures, it is hoped that these studies will further strengthen and promote the validity and competitiveness of laser-generated electron bremsstrahlung-driven research for the deduction of nuclear cross-sections of scientific relevance.

Acknowledgments

We thank the staff at the Institut für Optik und Quantenelektronik (IOQ) in Jena for their enthusiastic help during their experiments. This work was supported by the Atomic Weapons Establishment (AWE), Reading, UK and the Engineering and Physical Sciences Research Council (EPSRC).

References

[1] Ledingham K W D *et al* 2004 *J. Phys. D: Appl. Phys.* **37** 2341
[2] Snavely R A *et al* 2000 *Phys. Rev. Lett.* **85** 2945
[3] Robson L *et al* 2007 *Nat. Phys.* **3** 58
[4] Robinson A P L, Neely D, McKenna P and Evans R G 2007 *Plasma Phys. Control. Fusion* **49** 373
[5] McKenna P *et al* 2003 *Phys. Rev. Lett.* **91** 075006
[6] McKenna P *et al* 2005 *Phys. Rev. Lett.* **94** 084801
[7] Ledingham K W D, McKenna P and Singhal R P 2003 *Science* **300** 1107
[8] Ledingham K W D and Galster W *Rev. Mod. Phys.* to be published
[9] Mangles S P D *et al* 2005 *Phys. Rev. Lett.* **94** 245001
[10] Malka V *et al* 2002 *Science* **298** 1596
[11] Leemans W P, Nagler B, Gonsalves A J, Toth Cs, Nakamura K, Geddes C G R, Esarey E, Schroeder C B and Hooker S M 2006 *Nat. Phys.* **2** 696
[12] Liesfeld B, Amthor K-U, Ewald F, Schwoerer H, Magill J, Galy J, Lander G and Sauerbrey R 2004 *J. Phys. D: Appl. Phys.* **79** 1047
[13] Boyer K, Luk T S and Rhodes C K 1988 *Phys. Rev. Lett.* **60** 557
[14] Ledingham K W D *et al* 2000 *Phys. Rev. Lett.* **84** 899
[15] Cowan T E *et al* 2000 *Phys. Rev. Lett.* **84** 903
[16] Schwoerer H, Ewald F, Sauerbrey R, Galy J, Magill J, Rondinella V, Schenkel R and Butz T 2003 *Europhys. Lett.* **61** 47

[17] Spencer I *et al* 2002 *Rev. Sci. Instrum.* **73** 3801
[18] Cowan T E *et al* 2000 *Nucl. Instrum. Methods.* A **455** 130
[19] Ledingham K W D *et al* 2003 *J. Phys D: Appl. Phys.* **36** 79
[20] Magill J, Schwoerer H, Ewald F, Galy J, Schenkel R and Sauerbrey R 2003 *Appl. Phys.* B **77** 387
[21] Stoyer M A *et al* 2001 *Rev. Sci. Instrum.* **72** 767
[22] Haseltine E 2002 The 11 greatest unanswered questions of physics *Discover Magazine* **2** (February) 37
[23] Fasso A, Ferrari A, Ranft J and Sala P R 2005 *CERN Publication* INFN/TC 05/11, SLAC-R-773
[24] Gudowska I, Brahme A, Andreo P, Godowski W and Kierkegaard J 1999 *Phys. Med. Biol.* **44** 2099
[25] *IAEA Database* 2000 http://iaeand.iaea.org/photonuclear/index.html
[26] IAEA 2000 *TECDOC Handbook on Photonuclear Data for Applications, Appendix A Atlas of Giant Dipole Resonances* p 69
[27] *Experimental Nuclear Reaction Data (EXFOR CSISRS)* 2007 http://www.nndc.bnl.gov
[28] Herman M, Capote R, Carlson B, Oblozinsky P, Sin M, Trkov A and Zerkin V 2005 *EMPIRE Nuclear Reaction Model Code (version 2.19 Lodi)* http://www.nndc.bnl.gov/empire219/
[29] Young P G, Arthur E D and Chadwick M B 1996 *Proc. IAEA Workshop on Nuclear Reaction Data and Nuclear Reactors—Physics, Design and Safety* p 227
[30] Dietrich S S and Berman B L 1998 *At. Data Nucl. Data Tables* **38** 199
[31] Phillips T W, Cable M D, Cowan T E, Hatchett S P, Henry E A, Key M H, Perry M D, Sangster T C and Stoyer M A 1999 *Rev. Sci. Instrum.* **70** 1213
[32] Ishkhanov B S *et al* 1970 *J. Nucl. Phys.* **11** 272
[33] Wharton K B, Hatchett S P, Wilks S C, Key M H, Moody J D, Yanovsky V, Offenberger A A, Hammel B A, Perry M D and Joshi C 1998 *Phys. Rev. Lett.* **81** 822
[34] Malka G and Miquel J L 1996 *Phys. Rev. Lett.* **77** 75
[35] Clayton C E *et al* 1998 *Phys. Rev. Lett.* **81** 100
[36] Agostinelli S *et al* 2003 *Nucl. Instrum. Methods* A **506** 250
[37] Allison J *et al* 2006 *IEEE Trans. Nucl. Sci.* **53** 270
[38] Galy J, Maucec M, Hamilton D J, Edwards R and Magill J 2007 *New J. Phys.* **9** 23
[39] *MCNPX* 2005 http://mcnpx.lanl.gov and *LA-UR-03-1987* (revised 10 March 2005)
[40] Loiseau P 2007 *MSc-Report* ENSICAEN, Caen, France, to be published
[41] Schwoerer H, Gibbon P, Düsterer S, Behrens R, Ziener C, Reich C and Sauerbrey R 2001 *Phys. Rev. Lett.* **86** 2317
[42] Seltzer S M 1993 *Radiation Res.* **136** 147
[43] Hubbel J H and Seltzer S M 1996 http://physics.nist.gov/PhysRefData/XrayMassCoef/cover.html
[44] Spencer I *et al* 2001 *Nucl. Instrum. Methods* B **183** 449
[45] Norreys P A *et al* 1999 *Phys. Plasma* **6** 2150
[46] McCall G H 1982 *J. Phys. D: Appl. Phys.* **15** 823
[47] Behrens R, Schwoerer H, Düsterer S, Ambrosi P, Pretzler G, Karsch S and Sauerbrey R 2003 *Rev. Sci. Instrum.* **74** 961
[48] Cataldi M I C, Wolynec E, Martins M N, Gouffon P and Miyao Y 1988 *J. Phys. G: Nucl. Phys.* **14** 779
[49] Findlay D J S 1989 *Nucl. Phys.* A **276** 598
[50] Bergère R, Beil H and Veyssière A 1968 *Nucl. Phys.* A **121** 463
[51] Varlamov V V *et al* 2003 *At. Nauk. Tekh. Ser. Yad. Konst.* **1–2** 48
[52] Brown K L and Wilson R 1954 *Phys. Rev.* **93** 443
[53] Kneissl U, Koop E A, Kuhl G, Leister K H and Weller A 1975 *Nucl. Instrum. Methods* **127** 1
[54] Varlamov V V *et al* 1995 *Yad. Fiz.* **2** 1
[55] Drouin D, Couture A R, Joly D, Tastet X, Aimez V and Gauvin R 2007 *Scanning* **29** 92
[56] Kline F J and Hayward E 1978 *Phys. Rev.* C **17** 1531
[57] Martins M N, Hayward E, Lamaze G, Maruyama X K, Schima F J and Wolynec E 1984 *Phys. Rev.* C **30** 1855
[58] Teubner U *et al* 1996 *Phys. Rev.* E **54** 4167

[59] Amthor K-U, Liesfeld B, Ewald F, Schwoerer H, Sauerbrey R, Robson L, McKenna P and Ledingham K W D 2005 *Quantum Electron. Laser Sci. Conf.* **3** 1543
[60] Ivanchenko V G *et al* 1966 *Pisma ZHETF* **11** 452
[61] Carlos P, Beil H, Bergère R, Fagot J, Leprêtre A, Veyssière A and Solodukhov G V 1976 *Nucl. Phys.* A **258** 365
[62] Goryachev A M *et al* 1982 *Voprosy Teoreticheskoy i Yadernoy Fiziki* **8** 121
[63] Alvarez R A, Berman B L, Lasher D R, Phillips T W and Fultz S C 1971 *Phys. Rev.* C **4** 1673
[64] Dias J F, Martins M N and Wolynec E 1990 *Phys. Rev.* C **42** 1559
[65] Veyssière A, Beil H, Bergère R, Carlos P, Leprêtre A and de Miniac A 1974 *Nucl. Phys.* A **227** 513
[66] Fultz S C, Alvarez R A, Berman B L, Kelly M A, Lasher D R, Phillips T W and McElhinney J 1971 *Phys. Rev.* C **4** 149
[67] Ishkhanov B S, Kapitonov I M, Lazutin E V, Piskarev I M and Shevchenko V G 1972 *Nucl. Phys.* A **186** 438
[68] Varlamov V V *et al* 1979 *Yad. Fiz.* **30** 1185
[69] Ishkhanov B S, Kapitonov I M, Orlin V N, Piskarev I M, Shvedunov V I and Varlamov V V 1979 *Nucl. Phys.* A **313** 317
[70] Wyckoff J M, Ziegler B, Koch H W and Uhlig R 1965 *Phys. Rev.* **137** 576
[71] Sutton R, Thompson M N, Sugawara M, Shoda K, Saito T and Tsubota H 1980 *Nucl. Phys.* A **339** 125
[72] Thomas W 1925 *Naturwissenschaften* **13** 627
[73] Pywell R E and Thompson M N 1979 *Nucl. Phys.* A **318** 461
[74] Rodrigues T E, Arruda-Neto J D, Carvalheiro Z, Mesa J, Deppman A, Likhachev V P and Martins M N 2003 *Phys. Rev.* C **68** 014618
[75] Cook B C, Morrison R C and Schamber F H 1970 *Phys. Rev. Lett.* **25** 10 685
[76] Dogde W R, Leicht R G, Hayward E and Wolynec E 1981 *Phys. Rev.* C **24** 1952
[77] Beil H, Bergère R, Carlos P, Leprêtre A, de Miniac A and Veyssière A 1974 *Nucl. Phys.* A **219** 61
Beil H, Bergère R, Carlos P, Leprêtre A, de Miniac A and Veyssière A 1974 *Nucl. Phys.* A **227** 427
[78] Wagner A *et al* 2008 *J. Phys. G: Nucl. Phys.* **35** 014035
Wagner A *et al* 2007 *Preprint* 0707.3932
[79] Schwengner R *et al* 2007 *Nucl. Phys.* A **788** 331
[80] Strijckmans K 1999 http://users.ugent.be/ ~kstrykmn/nuclear/Coul_bar.txt
[81] Wagner A, Junghans A and Schwengner R 2006 http://www.fzd.de/db/Cms?pOid=24685&pNid=427